Research Report 2016-05

# Variability of regional extreme temperature over the Maritime Continent

Hongwei Yang

APCC
APEC CLIMATE CENTER

Research Report 2016-05

# Variability of regional extreme temperature over the Maritime Continent

Hongwei Yang

APCC
APEC CLIMATE CENTER

# PREFACE

To develop adaptation and mitigation strategies, the WCRP promoted a new set of coordinated climate model experiments CMIP5 to generate climate change projections world-wide. Consequently, CORDEX was organized as an international coordinated framework to produce an improved generation of regional climate change projections at local scale. Both global- and local-scale information on climate change is necessary in order to assess the impacts of these changes on human life and the natural environment. In CORDEX, multiple common domains covering all (or most) land areas in the world have been selected. CORDEX will produce an ensemble of multiple dynamical and statistical downscaling models that consider multiple forcing GCMs from the CMIP5 archive. The improved projections are to be used as inputs for impact and adaptation studies within AR5 of the IPCC timeline and beyond.

The Asia-Pacific Network, along with seven countries (Indonesia, Malaysia, Philippines, Thailand, Vietnam, Cambodia, and Lao PDR), has developed and funded the SEACLID project for three years, starting from October 2013. Taking advantage of SEACLID, CORDEX-SEA was established with the intention of providing improved high-resolution climate project information for local hydrological and agriculture sectors. APCC later joined the CORDEX-SEA project as one of the institutes from outside the SEA region.

Extreme temperature climate change information is studied in this report. This information is essential for analyzing the potential climatic impacts and adaptation measures for extreme climate events. Thus, the hindcast and historical downscaling experiments for the current climate were forced by reanalysis data and global model output, respectively in this study. Two climate change downscaling processes were driven by global model projections.

Hopefully, the results and data outputs of this study can provide application sectors with improved high-resolution climate change information that might eventually support the building of a long-term warning system. End-users and policy-makers will be able to weigh their response options based on these reliable local scale projections.

APCC will continue to promote the best use of our research outcomes in various theoretical and application areas. Our successes and achievements would not have been possible without the support of our valued partners. In addition to my appreciation to the APCC researchers, I extend my thanks to you and hope you enjoy this research report.

Dr. **Hong-Sang Jung**
President, APEC Climate Center
January 2017

# ABSTRACT

The frequency of extreme maximum (minimum) temperatures of hot days (cool nights) was analyzed over the Maritime Continent with data from observations, a dynamic downscaling of a hindcast experiment forced by the European Centre for Medium-Range Weather Forecasts Reanalysis-Interim dataset, a historical experiment forced by the Hadley Centre Global Environmental Model Version 2-Atmosphere-Ocean (HadGEM2-AO) global coupled model, near-future projections from a Representative Concentration Pathway (RCP) 4.5 experiment, and a far-future projection from an RCP 8.5 experiment forced by the future projections of the HadGEM2-AO output.

Correlations between observed extreme temperature frequency and the El Nino Southern Oscillation (ENSO) during hot or cool seasons were quantified over the local lands. We found that the impact of ENSO on extremes was dependent on the Madden-Julian Oscillation (MJO) phases. The overlapped downdraft anomaly of ENSO and MJO increased solar radiation during the daytime and outgoing longwave radiation during the nighttime, thus increasing the extreme events.

The hindcast experiment reasonably simulated the climate annual cycle of maximum and minimum temperature. Qualitatively, the impacts of ENSO and MJO on the frequency of hot days were reasonably reproduced in the hindcast experiment but not on the frequency of cool nights. The main features of extreme variation as a function of ENSO and MJO were generally comparable with observation.

Generally, the model produced realistic probability distributions of the extreme exceedance over all lands.

The historical experiment was capable of representing the phases of the annual cycle of maximum and minimum temperature, but the links between extreme temperature and ENSO or MJO were not very clear. The probability distributions of extreme exceedances were reasonably reproduced in the historical experiment.

There was a decreasing trend for slightly extreme hot day events in the future. However, the severely extreme hot days are often likely in the future. The extreme exceedance is likely to have a larger mean and spread in the future. The return period for all levels of extreme hot days is likely to become shorter in the future.

# CONTENTS

# 1. INTRODUCTION

The COordinated Regional climate Downscaling EXperiment (CORDEX) was established to improve the coordination of international efforts in regard to regional climate downscaling (RCD) research. The sophisticated circulation and thermodynamics forcing over the Maritime Continent (MC) create many difficulties for hydrological and agriculture management. Thus, the CORDEX-Southeast Asia (SEA) project was established recently over the MC to provide improved high-resolution climate project information for hydrological studies and the agriculture sector.

The MC is composed of thousands of islands, among which the Indo-China Peninsula (IC) and the Philippines are in the Northern Hemisphere (NH), Sumatra and Borneo are on the equator, and Java and New Guinea are in the Southern Hemisphere (SH), which represent extensive lands with large populations and economies. Climate change can have major impacts on society, the economy, and the environment. Future projections from the Coupled Model Intercomparison Project Phase 5 (CMIP5) models predict that the land surface temperature will likely increase 1.5-2°C in this region under Representative Concentration Pathway (RCP) 4.5 scenario by the end of the 21st century (Rogelj 2013).

Yang (2013, 2015) carried out dynamic downscaling research over the MC at both 50- and 25-km spatial resolutions. The experiment employing the 25-km grid outperformed the experiment employing the 50-km grid in many respects such as added values, spatial and temporal correlations, and root mean square errors. Yang (2015) analyzed the extreme precipitation in both observation and improved CORDEX-SEA experiments. However, extreme temperature in the improved experiments has not been studied because of limited resources.

It is well known that changes in extreme climate events have a disproportionate impact on society and ecosystems compared to changes in mean climate. Extreme temperature is especially important because this high-order statistical quantity is associated with large uncertainty and can severely impact the environment and economy. For example, SEA has been suffered an extended heat wave through much of April 2016 with temperatures reaching unprecedented levels. Thailand experienced the worst heat wave, with temperatures up to 44.6°C in 65 years (since 1950).

The hot weather in Cambodia was blamed for the death of an elephant trained to carry tourists at the famed Angkor Wat temple compound. Extreme temperatures during the hot season over the MC led to record energy consumption and prompted health warnings on everything from foodborne illness to drowning. Extreme temperature is the occurrence of temperatures above a threshold value (e.g., 90th percentile) near the upper end of the range of temperature.

The interannual variability over the MC is largely connected with the El Nino Southern Oscillation (ENSO) (Haylock and McBride 2001; Juneng and Tangang 2005). Kenyon and Hegerl (2008) found very strong influences of circulation on temperature extremes globally. Griffiths and Bradley (2007) found that changes in extremes in the northeast United States can be partly explained by ENSO using empirical orthogonal function (EOF) analysis. Gershunov and Barnett (1998) found that ENSO signals in the frequency of extreme warm temperature are found in the southern and eastern United States. Alexander et al. (2009) found that extreme maximum temperatures were significantly cooler during strong La Niña events than during strong El Niño events over Australia, southern Africa, India, and Canada while the converse was true for the United States and northeastern Siberia. These responses were larger when the effects of global warming were retained. Nicholls et al. (2005) found that the numbers of warm nights and hot days across most of the east Asia-west Pacific region increase substantially in the year after the onset of an El Niño event. The number of cool days and cold nights tend to decrease, although the relationship with El Niño is weaker for these variables. El Niño (La Niña) brings warmer (cooler) than normal conditions to SEA during the boreal winter (summer) (Deser and Wallace 1990). ENSO influences both maximum and minimum temperature variability, especially around the Pacific Rim, e.g., (Alexander et al. 2009; Kenyon and Hegerl 2008), but often affects cold and warm extremes differently.

In contrast, the Madden-Julian Oscillation (MJO) is the dominant mode of large-scale tropical intraseasonal variability (Madden and Julian 1994). Therefore, the MC climate is dominated by the MJO on intra-seasonal time scales (Hidayat and Kizu 2010; Wu et al. 2013). Observations show that extreme frequencies during active MJO periods are significantly higher than those in quiescent MJO phases in locations that are obviously influenced by the MJO (Jones et al. 2004).

Observational studies have showed significant increasing trends in the annual number of hot days and warm nights, with significant decreases in the annual number of cool days and cold nights over SEA (Griffiths et al. 2005; Manton et al. 2001). Tangang et al. (2016) also found a warming trend over Indonesia. Averaged over the country, the annual mean of daily maximum and minimum temperature had increased significantly by 0.18 and 0.30°C per decade, respectively. Nevertheless, links between extreme temperature and large-scale circulation modes over the MC have been studied less intensively than those over other regions, especially in the dynamic downscaling community.

In this study, we were motived to detect the impacts of ENSO and MJO on extreme temperature over the MC by analyzing the observation data first. The relationships between simulated extreme temperature and observed ENSO and MJO were than investigated. The probability distribution of extreme temperature is also discussed in this report.

The remainder of this report is organized as follows: We first introduce the data that was used in Section 2. The regional model and corresponding experimental design are described in Sections 3 and 4, respectively. Section 5 contains the results from the observations and hindcast, historical, and future projection experiments. The discussions and conclusion are presented in Section 6.

## 2. DATA

The daily maximum and minimum temperature from the Berkeley Earth project was used to analyze the observed extreme temperature events. The Berkeley data combines at least 16 datasets and is available from http://berkeleyearth.org/source-files/.

To investigate the influence of ENSO and MJO on extreme temperature over the SEA, indexes for both the ENSO and MJO were used. The Oceanic Nino Index (ONI), constructed from the extended reconstructed sea surface temperature (SST) data of the National Oceanic and Atmospheric Administration (NOAA) (Huang et al. 2015), was used to measure the El Niño and La Niña events. The NOAA interpolated outgoing longwave radiation (OLR) (Liebmann 1996) and zonal winds at 200 and 850 hPa from the National Centers for Environmental Prediction (NCEP) reanalysis II (Kanamitsu et al. 2002) were used to construct the MJO index according to Wheeler and Hendon (2004). Horizontal winds at 850 hPa, specific humidity at 700 hPa, and rainfall from NCEP reanalysis II were also used for analyzing the large-scale dynamics.

The European Centre for Medium-Range Weather Forecasts Reanalysis (ERA)-Interim (Berrisford et al. 2011; Dee et al. 2011) dataset was used for the large-scale forcing fields for the hindcast experiment. The output of the Hadley Centre Global Environmental Model Version 2-Atmosphere-Ocean (HadGEM2-AO) (Baek et al. 2013) was used as the forcing field for the historical (control) experiment and future projection experiments.

# 3. MODEL

The Weather Research and Forecast (WRF) 3.5 model, which is a primitive equation limited-area model under sigma coordinates, was used in this study. In general, the WRF is a regional prediction and downscaling system designed to meet both operational forecasting and atmospheric research needs. This system has advanced software architecture that allows for parallel computing and system extensibility. The development of state-of-the-art WRF technology was undertaken as a collaborative project by several organizations including the National Center for Atmospheric Research (NCAR), the Forecast Systems Laboratory, NOAA, NCEP, the Air Force Weather Agency (AFWA), the Naval Research Laboratory, the University of Oklahoma, and the Federal Aviation Administration. The WRF model allows researchers to conduct simulations reflecting either real data or idealized configurations and WRF is suitable for many applications at different scales ranging from meters to thousands of kilometers. Such applications include research and operational numerical weather prediction, data assimilation and parameterized physics research, downscaling climate simulations, driving air quality models, atmosphere-ocean coupling, and idealized simulations of phenomena such as boundary layer eddies, convection, and baroclinic waves. There are two dynamics solvers in the WRF Software Framework, namely, the Advanced Research WRF (ARW) solver (originally referred to as the Eulerian mass or “em” solver), which was developed primarily at NCAR, and the Nonhydrostatic Mesoscale Model solver, which was developed at NCEP. We employed the ARW solver in this study. The governing equations of the ARW dynamics solver are compressible, nonhydrostatic Euler equations. These equations are written in flux form, and their variables satisfy conservation equations following the philosophy of Ooyama (1990). Further, the equations are expressed using a terrain-following mass vertical coordinate system (Laprise 1992). In this model, the top surface is a constant pressure surface; we set the pressure of this surface to 50 hPa. Arakawa C-grid staggering was applied for the horizontal grid. A third order Runge Kutta scheme with a smaller time step for acoustic and gravity-wave modes was applied for time-split integration (Klemp and Wilhelmson 1978; Skamarock and Klemp 1992; Wicker and Skamarock 2002). The WRF model offers multiple physical options that can be combined in any way

(Skamarock et al. 2005).

In this study, we chose the WRF Single-Moment 6-Class Microphysics graupel scheme (Hong et al. 2004) for microphysics parameterization; this scheme includes six types of hydrometeors, namely, water vapor, cloud water, rain, cloud ice, snow, and graupel in six different arrays. Thus, it allows for the existence of supercooled water and a gradual melting of the snow below the melting layer. The scheme also introduced a new method for representing mixed-phase particle fall speeds weighted by the mixing ratios for the snow and graupel particles by assigning a single fall speed to both; this fall speed was applied to both sedimentation and accretion processes. We chose the modified Tiedtke scheme (Tiedtke 1989; Zhang et al. 2011) for cumulus parameterization; this scheme is a mass-flux type scheme that employs a convective available potential energy removal time scale, a shallow component, and momentum transport. Land surface parameterization follows the unified Noah land-surface model (Tewari et al. 2004), which is a unified NCEP/NCAR/AFWA scheme with soil temperature and moisture in four layers, fractional snow cover, and frozen soil physics. The Yonsei University (Hong et al. 2006) planetary boundary layer was employed here; in this technique, the counter gradient terms can be used to represent fluxes due to non-local gradients. The surface layer scheme was the Fifth-Generation Penn State/NCAR Mesoscale Model Monin-Obukhov scheme (Beljaars 1995; Dyer and Hicks 1970; Paulson 1970; Webb 1970; Zhang and Anthes 1982), which is based on the Monin-Obukhov scheme with a Carlson-Boland viscous sublayer and standard similarity functions from lookup tables. The longwave and shortwave radiative transfer model followed the Community Atmospheric Model (CAM) scheme (Collins et al. 2004), which is based on the CAM 3 climate model used in the Community Climate System Model; it takes into account the contributions of aerosols and trace gases and uses yearly carbon dioxide, constant nitrous oxide (311E-9), and methane (1714E-9).

The lateral boundary forcing fields included geopotential height, air temperature, specific humidity, and horizontal winds. The width of the buffer zone in our model was set to be 10 grid points, where the prognostic variables of the WRF model were nudged toward the large-scale forcing fields following the method of Davies and Turner (1977) with Newtonian nudging and horizontal diffusion within the regional climate model buffer zones. The following initial state conditions were used: surface pressure, sea-level pressure, 2-m height moisture, 2-m height temperature, 10-m height horizontal winds, soil moisture, soil temperature, and skin temperature. The skin temperature over the ocean was used as the SST. We obtained 30′ horizontal resolution topography and land use data for the Noah land surface model from the United States Geological Survey. The 30′ soil type data were obtained from the State Soil Geographic Database, and 5″ global data were obtained from the Food and Agriculture Organization of the United Nations.

# 4. EXPERIMENTAL DESIGN

The tropical climate over the MC is very important and unique because it is located in the most active convective area of the world and is influenced by both Hadley and Walker circulations. The MC consists of more than 10,000 islands with high topography.

To consider the climate system in this region, we needed (1) a sufficiently large domain size so that the regional model could develop its own dynamics and (2) sufficient computational resources; we designed our model domain covering the MC region to extend from 15° S to 27° N and from 90° to 145° E (Fig. 1). We chose the cylindrical equidistant map projection as the grid is close to rectangular in Euclid space over the tropical region. The zonal and meridional grid space was set to approximately 0.25° in order to adapt to the mesh resolution of observed data that were available for our study. The model had 221 west-east and 169 south-north grid points, and 37 sigma layers up to 50 hPa were used in the vertical direction.

Four experiments called the hindcast experiment, historical experiment, Down-45, and Down-85 were designed. The hindcast experiment was initiated and forced by the reanalysis dataset ERA-Interim, the historical experiment was forced by the HadGEM2-AO historical run, the Down-45 was forced by the HadGEM2-AO RCP 4.5, and the Down-85 was forced by the HadGEM2-AO RCP 8.5. The prescribed SST was from the same dataset of the lateral boundary forcing for each experiment. Here, the prefix "Down" in the experimental names refers to downscaling. The historical experiment was used as our control experiment, and its output was used as reference data for assessing the climate change. The ERA-Interim data are available at 6-h intervals with a horizontal resolution of 0.75° and 37 pressure levels. The output of HadGEM2-AO consists of 6-hourly data with a horizontal resolution of 1.25° for the latitude and 1.875° for the longitude. The enhanced greenhouse conditions were prescribed both in the lateral boundary conditions and inside of the model domain in Down-45 and Down-85. The physical parameterization scheme and model configuration were kept the same for all experiments. All model parameters were considered with their default values without tuning.

The hindcast experiment was run from 1 January 1980 to 31 December 2005. The historical experiment was run from 1 January 1970 to 31 December 2005. Down-45 and Down-85 were run from 1 January 2006 to 31 December 2100. The model outputs of the hindcast and historical experiments from 1981 to 2005 were analyzed. The near and far futures were defined as periods from 2021 to 2045 and from 2071 to 2095, respectively. The historical reference data for studying climate change was taken from the period 1981-2005, which is a subperiod of the historical experiment.

# 5. RESULTS

## 5.1 Observational analysis

In order to verify the ability of the WRF model to simulate extreme temperature events over the MC, we first investigated the correlations between extreme temperature and large-scale circulation patterns of ENSO and MJO in the observational dataset.

The daily maximum and minimum temperatures from the Berkeley Earth project were used to analyze the observed extreme temperature events. This dataset is a quality-controlled gridded dataset. Fig. 2 shows the climatology of the maximum and minimum temperatures (1979-2013), and the results clearly show the temperature peaks that likely contributed to the extreme events. Through the EOF analysis over individual land in IC, the Philippines, Sumatra, Borneo, Java, and New Guinea, homogeneous anomalous patterns for both maximum and minimum temperatures were found over all six lands (Fig. 3). The consistent peaks in climate-related maximum (minimum) temperature (Fig. 2) and the leading EOF pattern over individual regions (Fig. 3) confirmed that the separation of domains for maximum (minimum) temperature was reasonable for investigating extreme temperature. Therefore, over these six regions, the time series of the areal mean of the daily maximum (minimum) temperature were analyzed to find the links between extreme events and the large-scale circulation patterns of ENSO and MJO.

The base period for extreme events was 25 years from 1981 to 2005. The 90th (10th) percentile of daily maximum (minimum) temperature during the base period was used to distinguish extreme and normal maximum (minimum) temperature. Two indexes for extreme frequencies, i.e., TX90p and TN10p, were generated for each of the six lands by removing the climatological annual cycle of maximum and minimum temperatures, respectively. The frequency of extreme maximum temperature TX90p in the hot season and the frequency of extreme minimum temperature TN10p in the cool season have a great impact on nature and the socio-economic environment.

The warm days extreme index TX90p is defined as the percentage of days for which the daily maximum temperature is higher than the 90th percentile. Let $TX_{ij}$ be the daily maximum temperature on day i in period j and let $TX_{in}90$ be the calendar day 90th percentile centered on a 5-day window for the base period 1981-2005. The percentage of time for the base period is determined such that: $TX_{ij} > TX_{in}90$.

The cool days extreme index TN10p is defined as the percentage of days for which the daily minimum temperature is less than the 10th percentile. Let $TN_{ij}$ be the daily minimum temperature on day i in period j and let $TN_{in}$ 10 be the calendar day 10th percentile centered on a 5-day window for the base period 1981-2005. The percentage of time for the base period is determined such that: $TN_{ij} < TN_{in}90$. To avoid possible inhomogeneity across the in-base and out-base periods for both TX90p and TN10p, the calculation for the base period (1981-2005) requires the use of a bootstrap procedure. Details are described in (Zhang et al. 2005).

The weekly and monthly extreme temperature frequencies were both calculated because we wanted to determine the precursors of extreme events that might relate to low-frequency tropical intraseasonal variations and interannual variabilities.

To ensure our analysis focused only on hot seasons for TX90p and cool seasons for TN10p, the monthly climatological annual cycle of maximum (minimum) temperature were investigated to determine the hot (cool) seasons (Figs. 4 and 5).

As shown in Figs. 4 and 5, a hot season and cool season of the typical boreal monsoon climate clearly occurred in April-July (AMJJ) and December-February (DJF) over IC, where the monsoons began in April, matured in July-August, and retreated in October. Over the Philippines, a hot season (AMJJA) took place from April to August that started earlier than the boreal summer monsoon rains burst in the vicinity of the Philippines and finished when the monsoon retreated during August and September. The local cool season (JF) occurred typically in the boreal winter season. Over Sumatra, the hot season (FMAJJ) occured from February until July. The cool season (JAS) lasted from July and ended in September. Over Borneo, the hot season (AMJ) was between April and June, the cool season (JAS) occurred from July to September. Over Java, we chose two hot seasons (AM, SON) and two cool seasons (JA, JF) from the semiannual cycle of climatological temperature. Over New Guinea, the typical austral monsoon climate showed a hot season in

November-December-January (NDJ) and a cool season took place in July and August (JA). The north-easterly monsoon flow that crossed the equator turned north-westerly in December and brought plenty of moisture energy from the north-west Pacific. Generally over the MC, the amplitude of the annual cycle of temperature was small compared with that of extra tropics and high latitude regions. Therefore, the temperature difference between the hot and cool seasons was not that much. We tried to investigate the main seasons with relatively high or low temperatures for most lands in this study. In order to reflect the real features of the MC, two hot seasons and two cool seasons were chosen over Java.

The order of local hot seasons from north to south followed the smooth transition of the heating source from the Asian summer to Asian winter monsoon (Lau and Chan 1983; Meehl 1987; Tanaka 1994). The cool season occurred when the processes reversed. The seasonal cycle of temperature here is largely dominated by interactions between the complex terrain and the annual reversal of the surface monsoonal winds (Chang et al. 2005). Advection and radiative feedback processes dominated the maximum and minimum temperatures.

To find the link between extreme events and ENSO, the monthly extended reconstructed SST anomaly of NOAA based on the climatology in the base period from 1981-2005 was used to construct the ONI by calculating the time series over the Niño 3.4 region (5° N-5° S, 170°-120° W). El Niño (La Niña) is characterized by five consecutive 3-month running mean SST anomalies in the Niño 3.4 region that are above (below) the threshold of +0.5 (-0.5)°C.

Because the atmospheric response can lag El Niño by several months (Hegerl and Wallace 2002; Kenyon and Hegerl 2010), we attempted to study the lead-lag connection between ENSO and the extreme indexes of TX90p and TN10p. We selected the monthly TX90p (TN10p) in the hot (cool) seasons and the corresponding ONI during strong ENSO events (El Niño and La Niña events) in the lead-lag months for this purpose. During the calculation of the correlations, the weak ONI values (neither El Niño nor La Niña) were masked. The monthly TX90p (TN10p) out of the hot (cool) seasons was also masked. The correlation was calculated with those two masked monthly time series.

Table 1 presents the monthly correlation values between the observed TX90p in the local hot season and the ONI during El Niño and La Niña events over each of the six lands. We found that all the correlations were positive and most of them passed a 90% significant test. The correlations were relatively high over the lands where the hot season appeared in boreal spring or boreal summer. However the correlations were relatively low over the lands where the hot season appeared in boreal autumn or boreal winter.

The relation between extreme temperature and ENSO can be explained using capacitor theory (Xie et al. 2009). When ENSO matures in boreal winter, the signal can be stored in the Indian Ocean (IO). After ENSO decays in Mar to May, that stored signal begins to return to the Pacific Ocean, and the MC is on the pathway of those heat waves.

Hence, when the SST anomalies (SSTA) of El Niño over Niño 3.4 region reached their positive peak in the boreal winter, an anomalous positive energy was also stored in the IO. When the El Niño decayed in the following boreal spring, the heat waves stored in the IO transferred to the east and passed IC, the Philippines, Sumatra, Borneo, and Java, and therefore enhanced the local surface temperature in their hot seasons, i.e., TX90p was likely to increase. Thus, ONI was positively related with TX90p. For the hot seasons in the boreal autumn of Java and boreal winter of New Guinea, the ENSO signal must occur around the previous boreal later spring and early summer to match the long-term interannual variation of local maximum temperature. Although the SST over Niño 3.4 reached its maximum in the previous May, its interannual variation was relatively small, which might be the reason that the correlations between TX90p in the hot season of New Guinea and the second hot season of Java were low.

Table 2 presents the monthly correlation values between the observed -TN10p in local cool season and the ONI during El Niño and La Niña events over each of the six lands. When the temperature dropped in a specific cool season and the daily minimum temperature substantially decreased, extreme cool nights were likely to happen frequently, and the TN10p was likely to increase. Therefore, -TN10p maintained the same slop sign as the daily minimum temperature. For convenience, we used -TN10p instead of TN10p in the following study.

We found that only the negative correlation over IC passed a 90% significant test. Generally, the correlation was negative (positive) in boreal winter over the lands in the NH (SH), was positive (negative) in boreal summer over lands on equator (in the SH). For example, for IC and the Philippines in the NH, where the cool season occurs in boreal winter, after matching ENSO and the interannual variations of local minimum temperature, the leading developing phase of El Niño (or La Niña) dominated the boreal winter temperature anomaly over IC and the Philippines. When El Niño developed in autumn, the Niño 3.4 SSTA was positive and reached its peak in the following winter because of the accumulated energy. Meanwhile, the temperature anomaly dropped to its lowest values over IC and the Philippines, in addition to the minimum of the local annual cycle, so that -TN10p decreased to its lowest value. The situation was reversed for the La Niña case. Therefore, the correlation was negative. A similar explanation could be applied to other cases.

To detect the link between extreme events and the MJO, the daily NOAA Interpolated OLR and zonal winds at 200 and 850 hPa from the NCEP reanalysis II dataset were used to construct the MJO index (MJOI) according to Wheeler and Hendon (2004). In contrast to that index, we took an extended domain (-12.5°-25° N and 0°-360° E) according to the CORDEX-SEA project for convenience in our WRF downscaling study. The meridional averaging of the OLR and wind fields was skipped before the multivariate EOF analysis was carried out. The localized MJO index was reconstructed from the two leading principal components (PCs) of the multivariate EOF analysis and the two leading EOF patterns of the OLR field alone over each of the six lands. The MJO life cycle is shown in Fig. 6.

The correlation between MJOI and the frequency of hot days in the hot season and cool nights in the cool season was somewhat low, and therefore it is not shown here. However, the following composite study was conducted and produced meaningful results.

Fig. 7 shows the composited extreme frequency TX90p in the hot season as a function of eight MJO phases and two ENSO phases. Over all lands, the extreme frequency coherently varied with the extreme total (accumulated maximum temperature on hot days; figures not shown). To investigate the mechanism of the extreme frequency variation along the MJO and ENSO phases, the composited anomalies of OLR (olrA) and specific humidity at 700 mb (sh700A) over IC are shown in Fig. 7(a1) and 7(a2) according to the extreme frequency over IC in Fig. 7(a). When the olrA was somewhat large and decreased from MJO-1 to MJO-3 during El Niño conditions, the corresponding TX90p was also generally large and decreased from MJO-1 to MJO-3. However sh700A increased from MJO-1 to MJO-3. From MJO-3 to MJO-4, olrA showed an increasing trend, similarly to TX90p. The sh700A also changed differently. During MJO-5 and MJO-6, there were no hot days over IC in the hot season. The corresponding olrA and sh700A both showed no anomalies. TX90p occurred in MJO-7 while olrA also increased above zero. However, contrary to expectations, sh700A increased. In MJO-8, TX90p and olrA increased substantially and sh700A sharply decreased. Generally, the coherent change in TX90p and olrA, and inverse change between TX90p and sh700A also existed under La Niña conditions over IC, as well as under both El Niño and La Niña conditions over the other lands (figures for the olrA and sh700A are not shown). The exception of the increase in sh700A in MJO-7 might be due to the fact that the sh700A, as a proxy cloud anomaly, was the only dominant condition in cloudy weather to influence the surface temperature, in addition to the large latitude span from south to north over IC, which might be influenced differently by MJO.

Generally, the increased moisture over the land caused by advection was likely to block solar radiation and decrease the daytime temperature. The clear sky indicated by a large OLR value allows solar radiation to heat the ground as much as possible. Both the advective and radiative processes determined the surface temperature anomalies and thus the TX90p. A dynamical analysis of the MJO dependence with to the impact of ENSO on hot days, TX90p, is presented in the following paragraph.

Again, we use Fig. 7(a) over the IC as an example. During the first two MJO phases (MJO-1 and MJO-2), the El Niño event was more favorable for TX90p than La Niña conditions (Fig. 7(a)). This can be clearly seen in Fig. 8, which presents the anomalous evolution of the OLR and horizontal winds at 850 hPa as a function of MJO and ENSO conditionals on TX90p over IC. Similarly to Fig. 8, Fig. 9 shows the anomalous evolution of the rainfall as a function of MJO and ENSO conditionals on TX90p over IC. During MJO-1 and MJO-2, the anomalies of low level divergence and OLR were high over large area, thus the solar heating was stronger during El Niño conditions than those during La Niña conditions over IC. Consistently, the negative anomalous rainfall in El Niño conditions were stronger than those in La Niña conditions (Fig. 9). In this period, the MJO associated anomalous convection began over the Indian Ocean, and it gradually increased in strength and widened its spatial range to the southwest of MC (Fig. 6). However, during El Niño conditions, an anomalous subsidence of Walker circulation caused a low-level divergence over the MC and the surrounding ocean. This subsidence anomaly offset the low-level convergence anomaly produced by the active phase of the MJO over IC, which tended to strengthen the solar radiation for hot day generation. Conversely, during La Niña conditions, an anomalous weak ascent of Walker circulation over the MC enhanced the convection over IC and adjacent ocean. However, the MJO produced low level divergence over most of IC, which offset the weak convergence from La Niña and increased the positive olrA over most of IC. However the magnitude of positive olrA was smaller than the corresponding El Niño conditions. Therefore, the effect of radiative heating was smaller than the effects of El Niño conditions. Thus, TX90p under La Niña conditions was less than those under El Niño conditions.

Recall that the evolution of the large-scale circulation related to ENSO and MJO corresponding to the extremes, as shown in Fig. 8, only took place in IC. This could partly explain the distinct low or high extreme events of the nearby land, but not of all lands, because Fig. 8 is only conditional on the extremes over IC. The extremes over the other lands differed in timing from those over IC, so the phase differences in ENSO and MJO over each land must be one important reason for extreme events.

In MJO-3 and MJO-4, the convection anomaly associated with MJO moved farther east and became stronger over the south part of IC (Fig. 6). As most IC land is far from the equator relative to the other lands, the convection associated with MJO did not totally cover IC (Fig. 6). Therefore, the olrA associated with MJO was still positive during MJO-3 to MJO-4 and the corresponding rainfall anomaly was negative. During El Niño events, the subsidence over the MC offset convection strength over the southern MC and enhanced divergence over the northern area included most of IC in both MJO phases. However, the divergent anomaly over most parts of IC increased from MJO-3 to MJO-4 because the sample size increased from three to four days, which meant that the accumulated anomalies strengthened and therefore provide another explanation for the increased extreme temperatures from MJO-3 to MJO-4 in Fig. 7(a). The sample size was proportional to the accumulated anomalous divergent energy that quantified the extreme frequency of TX90p. The sample size in conjunction with the convergence and divergence patterns determined the change of extreme frequency in Fig. 7(a). In contrast to the data sampled under El Niño conditions, the sample size decreased to zero and two days during La Niña conditions, which decreased the accumulated anomalous divergence and so reduced the extremes in Fig. 7(a), even though the MJO divergence over IC in both MJO phases is near equally offset by the Walker circulation ascent anomaly in the MC.

In contrast to previous MJO phases, the sample size sharply decreased to zero in MJO-5 and MJO-6 during El Niño conditions. Actually, the MJO-5 was the most active phase and brought heavy rainfall over the MC (see the right column of Fig. 9), and it was associated with the strongest convective anomaly in that land of all the MJO phases. This anomalous ascent was generally stronger than the subsidence anomaly produced by El Niño over the southern IC. However, the increased speed of MJO at the MC when the cooling SST anomaly occurred during El Niño conditions was likely to reduce the chance of hot days. The opposite situation occurred in La Niña conditions, where the MJO slowed down at the MC when the warm SST anomaly occurred in La Niña conditions. Therefore, the sample size increased compared with those of the MJO-3 and MJO-4, and thus increased the TX90p in Fig. 7(a).

For MJO-7 during El Niño conditions, the MJO associated with the convergent anomaly moved further east and the accompanying divergent anomaly influenced the MC again. The sample size increased to two days because of the overlapped divergence of MJO and El Niño. In La Niña conditions, the associated convection overlapped the convection caused by MJO-7 and still controlled the climate over the Philippines and the adjacent area. That might have decreased the divergent strength over IC, reduced solar radiation in daytime, and thus reduced the occurrence of hot days. This might be the reason that TX90p was zero in that case. In MJO-8, the divergent flow associated with MJO dominated the climate over the MC again (Fig. 6). By further combining the subsidence of El Niño conditions, olrA and thus the solar radiation accumulated over 16 hot days of TX90p showed a strong positive olrA in MJO-8 under the El Niño conditions. Consistently, the strong negative rainfall anomaly occurred in MJO-8 under the El Niño conditions. Because of the offset effects of the convection from La Niña, the anomaly pattern over IC was very small, which reduced occurrence of hot days and thus TX90p was zero in the MJO-8 and La Niña case.

The anomalous evolution of the sh700A as a function of MJO and ENSO conditional on TX90p over the IC showed coherent variations as olrA and rainfall anomalies (figure not shown).

In regard to extremes over the other five lands, this type of evolution in large-scale circulation anomalies could be explained by a similar dynamic concept (figures not shown), except that the locations of convergence and divergence indicate phase shifting despite the different strengths. When the low-level divergence anomaly of MJO traveled eastward across the MC accompanied by its convergence counterpart, it encountered the subsidence (ascent) anomaly over the MC induced by the El Niño (La Niña) episode. The overlapped downdraft (updraft) anomaly would have enhanced (weaken) the local divergence and therefore allowed strong (weak) solar radiation to heat the ground and generate more (fewer) hot days; the combined effects of the opposite anomalies would have likely generated a normal frequency of hot days. Thus, the impact of ENSO on extreme temperature over the MC depended on the MJO phases. Generally, an El Niño episode was favorable for more hot days over MC.

Fig. 10 shows the composited extreme frequency TN10p in the cool season as a function of eight MJO phases and two ENSO phases. The advective and radiative physics were also the dominant processes that controlled the variation of TN10p. The anomalous evolution of the OLR and horizontal winds at 850 hPa as well as sh700A as a function of MJO and ENSO conditional on TN10p (figure not shown) demonstrate the similar concept that the overlapped downdraft anomaly associated with MJO and ENSO increases OLR in nighttime and cools the ground surface, thus increasing TN10p over the MC.

The coherent variation of the extremes in Fig. 7 and the anomalous large-scale circulation in Fig. 8 and sh700A (figure not shown) demonstrate that both dynamical and thermodynamical mechanisms dominated the extreme temperature over the tropical warm pool.

## 5.2 Hindcast experiment

Because of the complexity of land-sea contrasts, with several big islands higher than 2,000 m in the region, global models do not always resolve the important topographic features that determine the spatial variability of temperature at regional scales. The local error in the global model over the MC leads to systematic global uncertainties in medium-range weather predictions and climate simulations through planetary wave propagation (Peatman et al. 2014). However, a high-resolution model can capture the local features that arise from uplift condensation due to the topography (Qian and Zubair 2010), and this improves the predictive performance of the amplitude of the diurnal cycle and mean precipitation (Dirmeyer et al. 2012; Love et al. 2011; Wu and Hsu 2009) and even the ratio of stratiform to convective precipitation (Boyle and Klein 2010). Well simulated details of the convection system can improve the simulated energy budget at the ground surface, and therefore can increase the skill of model at simulating the surface temperature, especially the maximum and minimum temperature.

Thus, the CORDEX-SEA project was established with the intent of improving the coordination of international efforts in RCD research. The hindcast downscaling experiments for current climate were forced by the reanalysis data of ERA-Interim.

The climatological annual cycle in the hindcast experiment (Fig. 11 and 12) generally show reasonable results when compared with the results from observations (Fig. 4 and 5). Over IC, the hindcast experiment successfully simulated the seasonal progression of the boreal summer monsoon climate. The timing of monsoon onset (May), maturing (JJA), withdrawal (SO), and therefore the hot season (AMJJ in Fig. 11) and cool season (DJF in Fig. 12) were reasonably replicated. However, the regional model moderately underestimated the maximum temperature in the hot season, which may cause a lower occurrence of hot days in the model. The underestimated maximum temperature over the IC was mainly caused by the positive bias in the moisture flux convergence over the Bay of Bengal in the ERA-Interim dataset (Yang et al. 2012). The underestimated minimum temperature in the cool season in the hindcast experiment might increase cool nights in the model. Over the Philippines, maximum temperature was underestimated and minimum temperature was within the proper range in the model. Even though the maximum temperature in the hot season was not outstanding with respect to other months as in the observation and the minimum temperature in the hot season in the boreal later summer was still high relative to spring, which was different from the observed situation, our focus here was on finding the hot and cool seasons from the maximum and minimum temperature, respectively. The pronounced high maximum temperature during the hot season and low minimum temperature in the cool season relative to the other months in the hindcast experiment were consistent with the observations. Over Sumatra, the two semiannual cycles of maximum temperature in the observation showed different strength, while the second cycle was overestimated relative to the first cycle in the model, even though the maximum temperature for the all months was underestimated (Fig. 11). The magnitude of the minimum temperature was also underestimated in the hindcast experiment (Fig. 12). However, the cool season was still clear compared with the observation but with a relative overestimation of the minimum temperature in September. Generally, the timing of the hot and cool seasons was reasonable. Over Borneo, the peak of the semiannual cycle of the maximum temperature was clear. The hindcast experiment correctly simulated the timing of the semiannual cycles but underestimated the maximum temperature for all months. The model also always underestimated the minimum temperature, but its simulated semiannual cycle was better reproduced than that of the maximum temperature; therefore, the cool season was clearly distinguished from the other months. The clear variation in the maximum temperature semiannual cycle over Java was reasonably reproduced, with lower values relative to the observations. However, the two semiannual cycles were close to equal in the model. The annual cycle of minimum temperature was reasonable in the model with temperature that were lower than observation. The timing of the hot and cool seasons was reasonable. Over New Guinea, the seasonal progression of maximum and minimum temperatures themselves was reasonable, but lower quantities were obtained in the model simulations. Both the hot season and cool season were correctly simulated in the model from the maximum and minimum temperature, respectively.

Table 1 gives the correlations between extreme frequency TX90p in the hot season of the hindcast experiment and ONI in the El Niño and La Niña episodes. Four out of seven correlations between ONI and the TX90p passed a 90% significant test. The four correlations were for the Philippines, Sumatra, Borneo, and the first hot season over Java. Except over the IC, where the correlation was somewhat low, the regional model reasonably repeated the relationship between TX90p and the observed ENSO in the hot season.

Table 2 gives the correlations between extreme frequency TN10p in the cool season of the hindcast experiment and ONI in the El Niño and La Niña episodes. The correlations over the Philippines and Sumatra were relatively more reasonable than those over other lands. There was no correlation for the first cool season over Java because no cool days occurred in that case. Recall that there was a increasing trend of hot days and a decreasing trend of cool nights over the MC in the past decades. The increasing trend of TX90p iss adapting to global warming and might have robust relations with ENSO. However TN10p is not. Therefore, the relationship between TN10p and ENSO is relatively more sensitive than the relationship between TX90p and ENSO.

As a function of ENSO and MJO, the composited extreme frequency TX90p in the hot season is shown in Fig. 13. Over the IC, the regional model shows a different variation of extreme temperature frequency as a function of the ENSO and MJO phases than the observations (Fig. 13(a) and 7(a)). However, the following observed features were kept in the hindcast experiment: During MJO-1 and MJO-4, the El Niño conditions led to more hot days except when the model produced the same number of hot days under both the El Niño and La Niña conditions in MJO-3; During MJO-5 and MJO-6, the model produced more hot days under La Niña conditions than that under El Niño conditions; During MJO-7 and MJO-8, the model produced more hot days under El Niño conditions than under La Niña conditions. It produced an especially large number of hot days in the MJO-8 phase. Over the Philippines, the number of hot days produced by the model under El Niño conditions was not less than those produced under La Niña conditions during MJO-1 and MJO-4. The model produced more hot days under La Niña conditions in MJO-6, which was true in observation. However, the model overestimated the number of hot days in that case. Over Sumatra, it was reasonably simulated that El Niño was favourable for more hot days. However, the model underestimated the number of hot days in El Niño conditions in MJO-1. The number of hot days in La Niña conditions in all MJO phases were reasonably compared with the observed situation. Over Borneo, the model overestimated the number of hot days in El Niño conditions in MJO-3 compared with the observed number. Over Java, the model did not produce any hot days under El Niño conditions in MJO-3, while one hot day was observed. In MJO-7, observation showed one hot day in La Niña conditions, but the model missed that hot day. Instead, the model produced two hot days in MJO-8 under El Niño conditions, which were not observed. Over New Guinea, the model underestimated hot days under both ENSO phases during MJO-2 and MJO-3. Under El Niño conditions, the model produced more hot days than observed in MJO-7, while it produced fewer hot days in MJO-8. The model underestimated hot days under La Niña conditions in MJO-7.

As a function of ENSO and MJO, the composited extreme frequency TN10p in the cool season is shown in Fig. 14. Over IC, the variation of TN10p was reasonable under both ENSO phases compared with observation (Fig. 10a). Over the Philippines, the model reasonably produced cool nights not only in terms of variation under both ENSO phases but also with respect to the relatively higher or lower numbers for each MJO phase. Over Sumatra, the model obviously overestimated cool nights under El Niño conditions during MJO-2, MJO-4, and MJO-5. Over Borneo, the model underestimated cool nights under La Niña conditions in MJO-5 and MJO-6. Under El Niño conditions, the model underestimated cool nights in MJO-5 and overestimated cool nights in MJO-2, MJO-6, and MJO-7. Over Java, both the model and observation showed no cool nights under all phases of ENSO and MJO. Over New Guinea, the simulated MJO seems to shift one phase to the right. Otherwise, the model is likely to show better cool numbers compared with the observation.

Generally, the regional model is capable of simulating the extreme variations that occurred along with the changes in the MJO and ENSO. However, in many cases, the magnitudes of the extremes contained errors, which might have been due to the underestimation of both the maximum and minimum temperatures in the regional model. Extreme temperature involves higher-order statistics, and therefore the skill of the numerical models was generally poorer than it was for mean temperature. However, the model showed that an El Niño episode was generally favorable to more hot days and cool nights but depended on the MJO phases, which was consistent with the observed conclusion.

In addition, we analyzed the generalized extreme value probability density function (PDF) of extreme temperature over each of the six lands. Fig. 15 shows the PDFs fitted by a generalized Pareto distribution (Pickands III 1975) to the series of temperature exceedance of hot days during the base period. The robust means and variations are shown in the figure. Over IC, the hindcast experiment determined that both the mean and spread of extreme exceedance were equal to those of observation. The model underestimated both the mean and spread of the exceedance over the Philippines. Over Sumatra, the model slightly overestimated both the mean and spread of the exceedance. Over Borneo, the model slightly overestimated the mean but reproduced the spread of the exceedance. The model underestimated both the mean and spread of the exceedance over Java and New Guinea. Generally, the model produced realistic distributions of the exceedance over most lands, except the error was visually large over the Philippines.

Fig. 16 shows the PDFs fitted by a generalized Pareto distribution to the series of negative temperature exceedances of cool nights during the base period. The robust means and robust variations are shown in the figure. The model overestimated both the mean and spread of the exceedance over IC and New Guinea. Over the Philippines, the model overestimated the mean but underestimated the spread of the exceedance. The model underestimated both the mean and spread of the exceedance over Sumatra, Borneo, and Java. Generally the model produced realistic distributions of the exceedance over the Philippines, Sumatra, and Borneo. The error was only visually large over IC, Java, and New Guinea.

Generally, the regional model reasonably reproduced the phases of the climate annual cycle of maximum and minimum temperatures, but with a negative bias in the amplitude. Qualitatively, the impacts of ENSO on hot days were reasonably reproduced in the model except over IC. The impacts of ENSO on the cool nights in the model contained more uncertainty. As a function of the ENSO and MJO phases, the main features of the variations of extremes were generally acceptable compared with those in the observations. The magnitude and spread of extremes were realistic in the model.

## 5.3 Historical experiment

To conduct a climate change study for future scenarios with the CORDEX-SEA project, a historical experiment (control experiment) must be carried out that is forced by a global coupled model. Here, the global model was the HadGEM2-AO, which is same model used to force the future projection downscaling. The performance of the HadGEM2-AO was studied by (Baek et al. 2013).

First, we checked the climate annual cycle of maximum and minimum temperatures in the historical experiment (Fig. 17 and 18). The annual climate cycles of the maximum temperature in the historical experiment were generally reasonable compared with those in the observations (Fig. 4). Over IC, the historical experiment reasonably simulated the annual cycle of the boreal summer monsoon climate. The monsoon onset, maturing, withdrawal, hot season, and cool season were reasonably reproduced. However, the regional model underestimated the minimum temperature for all months and maximum temperature in the cool season. Over the Philippines, the annual cycle of the maximum temperature was clear but the hot season was longer in the historical experiment. The maximum temperature was underestimated for all months. The annual cycle of the minimum temperature was reasonable but the amplitude during May-July was underestimated relative to that during August -October. The timing of the cool season was correct. The range of the minimum temperature was better than that of the maximum temperature. Over Sumatra, the regional model unrealistically produced the semiannual cycle of the maximum temperature. However the first cycle had a larger amplitude than the second cycle, which was consistent with the observation. The maximum temperature in the first cycle changed much more quickly than the observation. The maximum temperature at the valley around July was relatively lower than the observation. The model underestimated the maximum temperature in all the months. The minimum temperature only showed one main peak in May and the cool period was flatter and longer than that in the observation. The model underestimated the minimum temperature in all months. Over Borneo, the variation of the semiannual cycle was similar to the observed cycle except that the amplitude of the maximum temperature was relatively lower in the first cycle than in the observation. Generally the maximum temperature was underestimated by the model. The model did not produce a clear annual cycle or semiannual cycle of minimum temperature over Borneo. More peaks and valleys were found in the model simulation than in the observation. Over Java, the semiannual cycle of the maximum temperature was not clear compared with the observation. The magnitude of the first cycle was relatively too large. Generally, the maximum temperature was underestimated by the model. The simulated phases and magnitude of the annual cycle of minimum temperature was quite good compared with that of the observation. Over New Guinea, the annual cycle of the maximum temperature was clear, but the maximum temperature was underestimated during January–March relative to that in November. The model underestimated the maximum temperature in all months compared with the observation. The model produced a clear annual cycle of the minimum temperature, and the timing of the cool season was correct. The simulated peak of the minimum temperature was late compared with that of the observation.

Second, we tried to find the links between extreme temperature in our historical experiment and the observed ENSO or MJO data. However, the results were unsatisfactory (data not shown). Although many studies have shown that temperature simulated in historical experiments with a global climate model (GCM) is reasonable, simulating large-scale circulation modes such as ENSO and MJO made it difficult to achieve the same level of skills in the historical experiments. When representing ENSO, the HadGEM2-AO missed the most extreme ENSO events, such as those in 1983, 1989, and 1998 (figure not shown). Nevertheless, the principal component (PC)1 and PC2 of the MJO index in the HadGEM2-AO barely showed any correlations with the PCs of observations (figure not shown). In fact, Leloup et al. (2008) showed that none of the GCMs in the Intergovernmental Panel on Climate Change Fourth Assessment Report database were sufficiently good at capturing all aspects of the extent, location, and timing of the ENSO events. This therefore seems to be a common shortcoming in CORDEX historical downscaling experiments given their dependence on the SSTA of coupled GCMs.

Even though the interannual and intraseasonal variation of extreme temperature in our historical experiment was unsatisfactory, we were able to investigate other aspects of the extremes such as the mean and spread. Fig. 15 compares the PDFs of extreme exceedance between the observations and historical experiment. The regional model in the historical experiment underestimated both the mean and spread of the extreme exceedance compared with the observation over IC, the Philippines, Sumatra, Borneo, and Java. Over New Guinea, the spread was also underestimated but the mean was the same as the observation. The largest error occurred over the Philippines.

Fig. 16 compares the PDFs of extreme exceedance between the observations and the historical experiment. The model overestimated the mean but underestimated the spread of the exceedance over IC and the Philippines. Moreover the model underestimated both the mean and spread of the exceedance over Borneo, Java, and New Guinea. Over Sumatra, the model overestimated the mean but simulated the same spread compared with the observation.

In future studies, a multi-model ensemble of all the CORDEX-SEA data needs to be considered to find the reliable and robust extreme temperature events in historical downscaling experiments.

## 5.4 Future projections

The sophisticated circulation and thermodynamic forcing over the MC creates many difficulties for hydrological and agriculture management. In particular, high-resolution information is necessary for developing warning systems, and this can be derived from fine-grid experiments that not only reflect the important topographic effects, but also project consistent signs of climate change (Smith et al. 2013). Thus, extreme temperature downscaling with a regional model is an important approach to studying fine-scale climate changes in projected scenarios (Christensen and Christensen 2004; Eun-Soon and Kwon 2007; Fowler et al. 2007; Im et al. 2007).

Projected extreme temperature changes imply possible heat waves over tropical regions. Several studies have mentioned that extreme temperature will likely increase in the 21st century over many areas of the globe, such as over the West Pacific (Cai et al. 2012), Korea (Im et al. 2007), and tropical regions (Seneviratne et al. 2012). However, extreme temperature change research over SEA has been studied less intensively than that over other regions.

To analyze changes in extremes in future projections with Down-45 and Down-85 in our study, we selected two cases to evaluate the differences from the historical experiment. Specifically, the near future of Down-45 and far future of Down-85 were chosen to investigate the impact of greenhouse gas emissions as the situation worsens over time.

The changes in extreme temperature could be detected by the probability distribution (Fig. 19). The shifting of generalized Pareto distributions for the Down-45 and Down-85 experiments relative to that in the historical experiments explained or inferred the changes in the mean and variation of extreme temperature. Over IC, the Down-45 produced a slightly larger mean and spread of extreme exceedance than those in the historical experiments. In addition the Down-85 produced quite a large increase in both the mean and spread of exceedance in the far future. A similar change is likely to happen in the future over all other five lands. Slightly extreme events are likely to decrease in the future. However, severe extreme events are likely to increase in the future, especially in the Down-85.

For TN10p, the increased trend of minimum temperature made the sample size very small, especially in the experiment for Down-85. Therefore, the few cool nights did not have a well-fitted function, and we did not show the figures.

In this study, we assessed possible changes in the near-future (RCP 4.5; 2021-2045) and far-future (RCP 8.5; 2071-2095) extreme temperature values through return period analysis over the MC. The return value for a return period of T days is defined as the temperature that is exceeded by a daily extreme with a probability of 1/T. A return period is the average interval between events of the same magnitude. In this study, we analyzed the return values of daily extreme temperature exceedance with recurrences within 100 days. Hence, the threshold for a return period of 100 days is the temperature exceedance that would be expected once every 100 days. The return values for return periods in excess of 100 days were considered less reliable because there were few samples for very extreme temperatures corresponding to longer return periods and thus the results were not presented here. In our study, the return period for extreme temperature was considered over the all years.

Fig. 20 compares the return value versus return period for the future projections and our historical experiment. Over IC, we wanted to look at the large return values that could critically impact society, for example, periods with return values higher than 2 K. The return period became shorter in the Down-45 and even shorter in the Down-85. For extreme events with exceedances of 2 K, the return period was around 45 days in the years simulated by the historical experiment, while it was shortened to 15 days in the Down-45 and about three days in the Down-85 projections. Similar to IC, the return period became shorter in the future over all the other five lands.

Note that the dynamical and thermodynamic mechanism were equally important to control the extreme temperature over the tropical warm pool. The shortened return period might be due to a circulation change, which could reduce the water vapor supply in the convergence band and increase the solar radiation.

# 6. CONCLUSION AND DISCUSSION

In this study, we analyzed the extreme temperature of hot days in the hot season and cool nights in the cool season over the MC from observations, dynamic downscaling of a hindcast experiment forced by the ERA-Interim reanalysis dataset, a historical experiment forced by the HadGEM2-AO global coupled model, and downscaling for near-future RCP4.5 and far-future RCP8.5 projections forced by the HadGEM2-AO output.

We quantified the correlation between strong ENSO events and the extreme temperature frequency TX90p in the hot season (TN10p in the cool season). TX90p was highly influenced by ENSO in the boreal spring and summer hot season and most the correlations passed a 90% significant test. However, the correlation in the austral spring and summer showed relatively low values over the lands in the SH. In case of the link between ENSO and TN10p, the correlation was generally negative (positive) in the boreal winter over the lands on the NH (SH), and was positive (negative) in the boreal summer over lands on the equator (SH). The absolute correlation over the Philippines, Sumatra, and Borneo were relatively low.

We conducted a composite analysis according to strong ENSO and MJO phases during the local hot (cool) season over the MC lands from 1981-2005. We found that an El Niño episode was favorable for extreme temperatures for both hot days and cool nights. However the impact of ENSO on extremes was dependent on the MJO phases. When the low level divergence anomaly of MJO traveled eastward across the MC accompanied by its convergence counterpart, it encountered a subsidence (ascent) anomaly over the MC induced by the El Niño (La Niña) episode. The overlapped downdraft (updraft) anomaly would have enhanced (weakened) the local divergence and therefore allowed strong (weak) solar radiation to heat the ground in daytime and strong OLR to cool the ground during the nighttime, thus generating more (less) extremes temperature for both TX90p and TN10p; the combined effects of the opposite anomalies would have likely generated a moderate frequency of extreme events.

Generally in the hindcast experiment, the regional model reasonably reproduced the phases of the climate annual cycle for maximum and minimum temperatures, but with biases in the amplitude. Qualitatively, the regional model reasonably repeated the relationship between TX90p and the observed ENSO in the hot season in terms of the correlation coefficient except over the IC. The relationship between TN10p and ENSO was relatively more sensitive and uncertain than that between TX90p and ENSO. As a function of the ENSO and MJO phases, the variations of extremes were comparable with that in the observations. However, the frequency of extremes contained errors in many cases, which might have been due to the underestimation of both maximum and minimum temperatures in the regional model. However, the model showed that an El Niño episode was generally favorable to more hot days and cool nights but depended on the MJO phases, which was consistent with the observed conclusion. Generally the model produced realistic probability distributions of the extreme exceedance over all lands.

The climatological annual cycles in the historical experiment were generally reasonable in terms of phases compared with those in the observations. However, the links between the extreme temperature and ENSO or MJO were unsatisfactory, which was caused by the unrealistic representation of ENSO and MJO in the large-scale forcing of HadGEM2-AO compared to the observed ENSO and MJO. In future studies, the links between model extremes and model ENSO or MJO need to be investigated to show the model dynamics for the extremes that were impacted by the large circulation mode. In most cases, the probability distributions of extreme exceedance were reasonably reproduced in the historical experiment.

In the downscaling experiments for future projections, the Down-45 produced a slightly larger mean and spread of extreme exceedance than those in the historical experiments. Meanwhile, the Down-85 produced a quite large increase for both the mean and spread of exceedance in the far future. The slight extreme events are likely to decrease in the future. However, severely extreme events are likely to increase in the future. The return period for any level of extreme hot days is likely to become shorter in the future over all the lands.

Our analysis was based on the regional temperature extremes, which reduced the uncertainty. In contrast, robust mean and robust standard deviation were calculated when the probability distribution was estimated, which decreased the uncertainty in another way. Even though, the uncertainty remains there in our study.

However, Zwiers et al. (2013) noticed that the trends of temperature extremes are broadly similar, even though some kinds of uncertainties existed in the observational data.

As pointed out in the results, the historical experiment looks very limited mainly because of the serious SST bias and poor ENSO performance in HadGEM2-AO. To make our results more robust, the TX90p (TN10p) of our historical experiment and future projection were compared with extremes from some the Coupled Model Intercomparison Project (CMIP)5 models. The downscaled extremes are generally within the spread of the CMIP5 models.

A multimodel ensemble of all the CORDEX-SEA project data needs to be considered in future studies to provide further reliable and robust estimates of extreme temperature and its links to large-scale precursors in the model results.

## Acknowledgements

I would like to thank the three reviewers for their insightful and constructive suggestions. In addition, Prof. Ahn at Pusan National University and Prof. Chang at Kongju National University are also appreciated for their help.

## REFERENCE

Alexander L.V., Uotila P., Nicholls N. (2009) Influence of sea surface temperature variability on global temperature and precipitation extremes. J Geophys Research: Atmospheres

Baek H.-J., Lee J., Lee H.-S., Hyun Y.-K., Cho C., Kwon W.-T., Marzin C., Gan S.-Y., Kim M.-J., Choi D.-H., others (2013) Climate change in the 21st century simulated by HadGEM2-AO under representative concentration pathways. Asia-Pacific J Atmos Sci 49:603-618

Beljaars A. (1995) The parametrization of surface fluxes in large-scale models under free convection. Q J R Meteorol Soc 121:255-270

Berrisford P., Kallberg P., Kobayashi S., others (2011) The ERA-Interim archive version 2.0.

Technical Report, 23 European Centre for Medium-Range Weather Forecasts

Boyle J., Klein S.A. (2010) Impact of horizontal resolution on climate model forecasts of tropical precipitation and diabatic heating for the TWP-ICE period. J Geophys Research: Atmospheres

Cai W., Lengaigne M., Borlace S., Collins M., Cowan T., McPhaden M.J., Timmermann A., Power S., Brown J., Menkes C., others (2012) More extreme swings of the South Pacific convergence zone due to greenhouse warming. Nature 488:365-369

Chang C.-P., Wang Z., McBride J., Liu C.-H. (2005) Annual cycle of Southeast Asia-Maritime Continent rainfall and the asymmetric monsoon transition. J Clim 18:287-301

Christensen O.B., Christensen J.H. (2004) Intensification of extreme European summer precipitation in a warmer climate. Glob Planetary Chang 44:107-117

Collins W.D., Rasch P.J., Boville B.A., Hack J.J., McCaa J.R., Williamson D.L., Kiehl J.T., Briegleb B., Bitz C., Lin S.J., others (2004) Description of the NCAR community atmosphere model (CAM 3.0). Ncar Tech. Note Ncar/Tn-464+ Str

Davies H.C., Turner R_E. (1977) Updating prediction models by dynamical relaxation: An examination of the technique. Q J R Meteorol Soc 103:225-245

Dee D.P., Uppala S.M., Simmons A.J., Berrisford P., Poli P., Kobayashi S., Andrae U., Balmaseda M.A., Balsamo G., Bauer P., others (2011) The ERA-Interim reanalysis: Configuration and performance of the data assimilation system. Q J R Meteorol Soc 137:553-597

Deser C., Wallace J.M. (1990) Large-scale atmospheric circulation features of warm and cold episodes in the tropical Pacific. J Clim 3:1254-1281

Dirmeyer P.A., Cash B.A., Kinter III J.L., Jung T., Marx L., Satoh M., Stan C., Tomita H., Towers P., Wedi N., others (2012) Simulating the diurnal cycle of rainfall in global climate models: Resolution versus parameterization. Clim Dyn 39:399-418

Dyer A.J., Hicks B.B. (1970) Flux-gradient relationships in the constant flux layer. Q J R Meteorol Soc 96:715-721

Eun-Soon I., Kwon W.-T. (2007) Characteristics of extreme climate sequences over Korea using a regional climate change scenario. Sola 3:17-20

Fowler H.J., Ekström M., Blenkinsop S., Smith A.P. (2007) Estimating change in extreme European precipitation using a multimodel ensemble. J Geophys Research: Atmospheres

Gershunov A., Barnett T.P. (1998) ENSO influence on intraseasonal extreme rainfall and temperature frequencies in the contiguous United States: Observations and model results. J Clim 11:1575-1586

Griffiths G.M., Chambers L.E., Haylock M.R., Manton M.J., Nicholls N., Baek H.-J., Choi Y., Della-Marta P.M., Gosai A., Iga N., others (2005) Change in mean temperature as a predictor of extreme temperature change in the Asia-Pacific region. Int J Climatol 25:1301-1330

Griffiths M.L., Bradley R.S. (2007) Variations of twentieth-century temperature and precipitation extreme indicators in the northeast United States. J Clim 20:5401-5417

Haylock M., McBride J. (2001) Spatial coherence and predictability of Indonesian wet season rainfall. J Clim 14:3882-3887

Hegerl G.C., Wallace J.M. (2002) Influence of patterns of climate variability on the difference between satellite and surface temperature trends. J Clim 15:2412-2428

Hidayat R., Kizu S. (2010) Influence of the Madden-Julian Oscillation on Indonesian rainfall variability in austral summer. Int J Climatol 30:1816-1825

Hong S.-Y., Dudhia J., Chen S.-H. (2004) A revised approach to ice microphysical processes for the bulk parameterization of clouds and precipitation. Mon Weather Rev 132:103-120

Hong S.-Y., Noh Y., Dudhia J. (2006) A new vertical diffusion package with an explicit treatment of entrainment processes. Mon Weather Rev 134:2318-2341

Huang B., Banzon V.F., Freeman E., Lawrimore J., Liu W., Peterson T.C., Smith T.M., Thorne

P.W., Woodruff S.D., Zhang H.-M. (2015) Extended reconstructed sea surface temperature version 4 (ERSST. v4). Part I: upgrades and intercomparisons. J Clim 28:911-930

Im E.-S., Kim M.-H., Kwon W.-T., Steven C. (2007) Projected change in mean and extreme climate over Korea from a double-nested regional climate model simulation. J Meteorol Soc Jpn 85:717-732

Jones C., Waliser D.E., Lau K.M., Stern W. (2004) Global occurrences of extreme precipitation and the Madden-Julian Oscillation: Observations and predictability. J Clim 17:4575-4589

Juneng L., Tangang F.T. (2005) Evolution of ENSO-related rainfall anomalies in Southeast Asia region and its relationship with atmosphere-ocean variations in Indo-Pacific sector. Clim Dyn 25:337-350

Kanamitsu M., Ebisuzaki W., Woollen J., Shi-Keng Y., others (2002) Ncep-doe amip-ii reanalysis (r-2). Bull Am Meteorol Soc 83:1631

Kenyon J., Hegerl G.C. (2008) Influence of modes of climate variability on global temperature extremes. J Clim 21:3872-3889

Kenyon J., Hegerl G.C. (2010) Influence of modes of climate variability on global precipitation extremes. J Clim 23:6248-6262

Klemp J.B., Wilhelmson R.B. (1978) The simulation of three-dimensional convective storm dynamics. J Atmos Sci 35:1070-1096

Laprise R. (1992) The Euler equations of motion with hydrostatic pressure as an independent variable. Mon Weather Rev 120:197-207

Lau K.M., Chan P.H. (1983) Short-term climate variability and atmospheric teleconnections from satellite-observed outgoing longwave radiation. Part II: Lagged correlations. J Atmos Sci 40:2751-2767

Leloup J., Lengaigne M., Boulanger J.-P. (2008) Twentieth century ENSO characteristics in the IPCC database. Clim Dyn 30:277-291

Liebmann B. (1996) Description of a complete (interpolated) outgoing longwave radiation dataset. Bull. Amer. Meteor. Soc. 77:1275-1277

Love B.S., Matthews A.J., Lister G. (2011) The diurnal cycle of precipitation over the Maritime Continent in a high-resolution atmospheric model. Q J R Meteorol Soc 137:934-947

Madden R.A., Julian P.R. (1994) Observations of the 40-50-day tropical oscillation-A review.

Mon Weather Rev 122:814–837

Manton M.J., Della–Marta P.M., Haylock M.R., Hennessy K.J., Nicholls N., Chambers L.E., Collins D.A., Daw G., Finet A., Gunawan D., others (2001) Trends in extreme daily rainfall and temperature in Southeast Asia and the South Pacific: 1961–1998. Int J Climatol 21:269–284

Meehl G.A. (1987) The annual cycle and interannual variability in the tropical Pacific and Indian Ocean regions. Mon Weather Rev 115:27–50

Nicholls N., Baek H.–J., Gosai A., Chambers L.E., Choi Y., Collins D., Della–Marta P.M., Griffiths G.M., Haylock M.R., Iga N., others (2005) The El Nino–Southern Oscillation and daily temperature extremes in east Asia and the west Pacific. Geophys Res Lett

Ooyama K.V. (1990) A thermodynamic foundation for modeling the moist atmosphere. J Atmos Sci 47:2580–2593

Paulson C.A. (1970) The mathematical representation of wind speed and temperature profiles in the unstable atmospheric surface layer. J Appl Meteorol 9:857–861

Peatman S.C., Matthews A.J., Stevens D.P. (2014) Propagation of the Madden–Julian Oscillation through the Maritime Continent and scale interaction with the diurnal cycle of precipitation. Q J R Meteorol Soc 140:814–825

Pickands III J. (1975) Statistical inference using extreme order statistics. Annals Statistics pages 119–131

Qian J.–H., Zubair L. (2010) The effect of grid spacing and domain size on the quality of ensemble regional climate downscaling over South Asia during the northeasterly monsoon. Mon Weather Rev 138:2780–2802

Rogelj J. (2013) Long–term climate change: projections, commitments and irreversibility. Cambridge University Press

Seneviratne S.I., Nicholls N., Easterling D., Goodess C., Kanae S., Kossin J., Luo Y., Marengo J., McInnes K., Rahimi M., others (2012) Managing the risks of extreme events and disasters to advance climate change adaptation a special report of Working Groups I and II of the Intergovernmental Panel on Climate Change (IPCC). Cambridge University Press, Cambridge, UK, and New York, NY, USA, Ch. Changes in climate extremes and their impacts on the natural physical environment

Skamarock W.C., Klemp J.B. (1992) The stability of time–split numerical methods for the hydrostatic and the nonhydrostatic elastic equations. Mon Weather Rev 120:2109–2127

Skamarock W.C., Klemp J.B., Dudhia J., Gill D.O., Barker D.M., Wang W., Powers J.G.

(2005) A description of the advanced research WRF version 2. Technical Report, DTIC Document

Smith I., Moise A., Katzfey J., Nguyen K., Colman R. (2013) Regional-scale rainfall projections: Simulations for the New Guinea region using the CCAM model. J Geophys Research: Atmospheres 118:1271-1280

Tanaka M. (1994) The onset and retreat dates of the Austral summer monsoon over Indonesia, Australia and New Guinea. J Meteorol Soc Jpn 72:255-267

Tangang F., Juneng L., Aldrian E. (2016) Observed changes in extreme temperature and precipitation over Indonesia. Int J Climatol

Tewari M., Chen F., Wang W., Dudhia J., LeMone M.A., Mitchell K., Ek M., Gayno G., Wegiel J., Cuenca R.H. (2004) Implementation and verification of the unified NOAH land surface model in the WRF model. 20th conference on weather analysis and forecasting/16th conference on numerical weather prediction pages 11-15

Tiedtke M. (1989) A comprehensive mass flux scheme for cumulus parameterization in large-scale models. Mon Weather Rev 117:1779-1800

Webb E.K. (1970) Profile relationships: The log-linear range, and extension to strong stability. Q J R Meteorol Soc 96:67-90

Wheeler M.C., Hendon H.H. (2004) An all-season real-time multivariate MJO index: Development of an index for monitoring and prediction. Mon Weather Rev 132:1917-1932

Wicker L.J., Skamarock W.C. (2002) Time-splitting methods for elastic models using forward time schemes. Mon Weather Rev 130:2088-2097

Wu C.-H., Hsu H.-H. (2009) Topographic influence on the MJO in the Maritime Continent. J Clim 22:5433-5448

Wu P., Arbain A.A., Mori S., Hamada J.-i., Hattori M., Syamsudin F., Yamanaka M.D. (2013) The effects of an active phase of the Madden-Julian oscillation on the extreme precipitation event over western Java Island in January 2013. Sola 9:79-83

Xie S.-P., Hu K., Hafner J., Tokinaga H., Du Y., Huang G., Sampe T. (2009) Indian Ocean capacitor effect on Indo-western Pacific climate during the summer following El Niño. J Clim 22:730-747

Yang H.-W. (2013) Revision of climate change by dynamic downscaling over the maritime continents. Technical Report, APEC Climate Center

Yang H.-W. (2015) Dynamic downscaling of climate change over the maritime continents.

Technical Report, APEC Climate Center

Yang H.-W. (2015) Regional precipitation extremes over the maritime continent. Technical Report, APEC Climate Center

Zhang C., Wang Y., Hamilton K. (2011) Improved representation of boundary layer clouds over the Southeast Pacific in ARW-WRF using a modified Tiedtke cumulus parameterization scheme. Mon Weather Rev 139:3489-3513

Zhang D., Anthes R.A. (1982) A high-resolution model of the planetary boundary layer-sensitivity tests and comparisons with SESAME-79 data. J Appl Meteorol 21:1594-1609

Zhang X., Hegerl G., Zwiers F.W., Kenyon J. (2005) Avoiding inhomogeneity in percentile-based indices of temperature extremes. J Clim 18:1641-1651

Zwiers F.W., Alexander L.V., Hegerl G.C., Knutson T.R., Kossin J.P., Naveau P., Nicholls N., Schär C., Seneviratne S.I., Zhang X. (2013) Climate extremes: challenges in estimating and understanding recent changes in the frequency and intensity of extreme climate and weather events. Springer

# TABLES

**Table 1** Monthly correlation between TX90p (in hot months in the observation and hindcast experiment) and observed ONI (during El Niño and La Niña events) over IC, the Philippines, Sumatra, Borneo, Java, and New Guinea. Numbers marked with "*" mean that the correlation passed the 90% significant test.

| Correlation | Obs | Hindcast | Hot season | Lead month |
|---|---|---|---|---|
| IC | 0.50* | 0.14 | 4–7 | 4 |
| Philippines | 0.53* | 0.39* | 4–8 | 5 |
| Sumatra | 0.64* | 0.59* | 2–6 | 4 |
| Borneo | 0.49 | 0.62* | 4–6 | 2 |
| Java | 0.62*/0.08 | 0.71*/0.17 | 4–5/9–11 | 3 |
| New Guinea | 0.19 | 0.32 | 11–1 | 7 |

**Table 2** Monthly correlation between TN10p (in the cool months in the observation and hindcast experiment) and observed ONI (during El Niño and La Niña events) over IC, the Philippines, Sumatra, Borneo, Java, and New Guinea. Numbers marked with "*" mean that the correlation passed the 90% significant test.

| Correlation | Obs | Hindcast | Cool season | Lead month |
|---|---|---|---|---|
| IC | −0.63* | 0.14 | 12–2 | 5 |
| Philippines | −0.28 | −0.12 | 1–2 | 7 |
| Sumatra | 0.27 | 0.37 | 7–9 | 4 |
| Borneo | 0.24 | −0.42 | 7–9 | 4 |
| Java | −0.97/0.64 | None/−0.34 | 7–8/1–2 | 5 |
| New Guinea | −0.47 | −0.01 | 7–8 | 6 |

# FIGURES

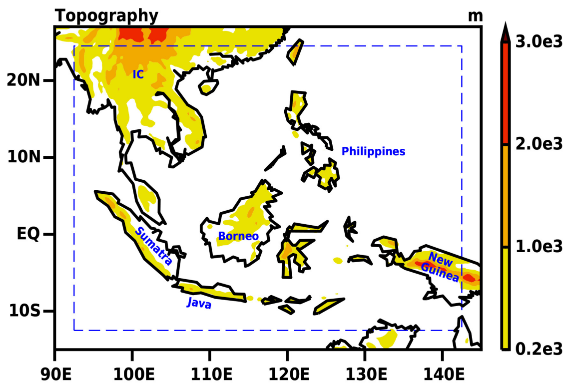


Figure 1 Domain (15° S–27° N, 90°–145° E), buffer zone (outside of the blue dashedrectangle: 12.5° S–24.5° N, 87.5°–142.5° E ), and topography (color shades are in units ofmeters). Analysis areas over land enclosed by the blue rectangle refer to IC, Sumatra,Java, Borneo, New Guinea, and the Philippines.

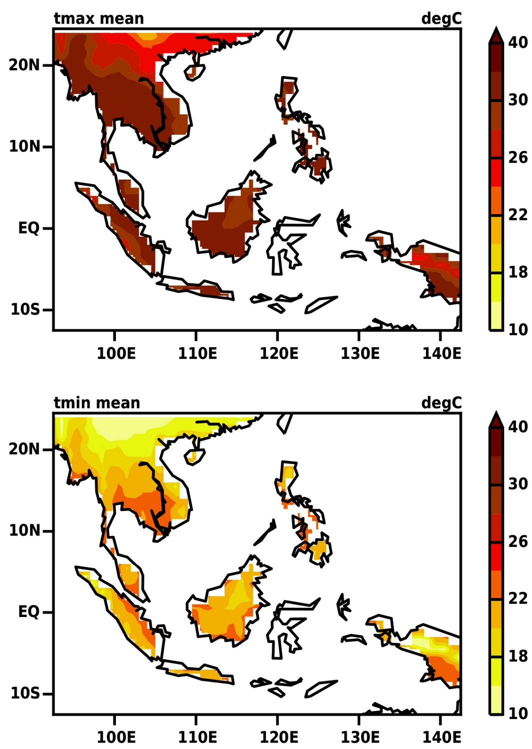


Figure 2 Climatological maximum and minimum temperature of daily data.

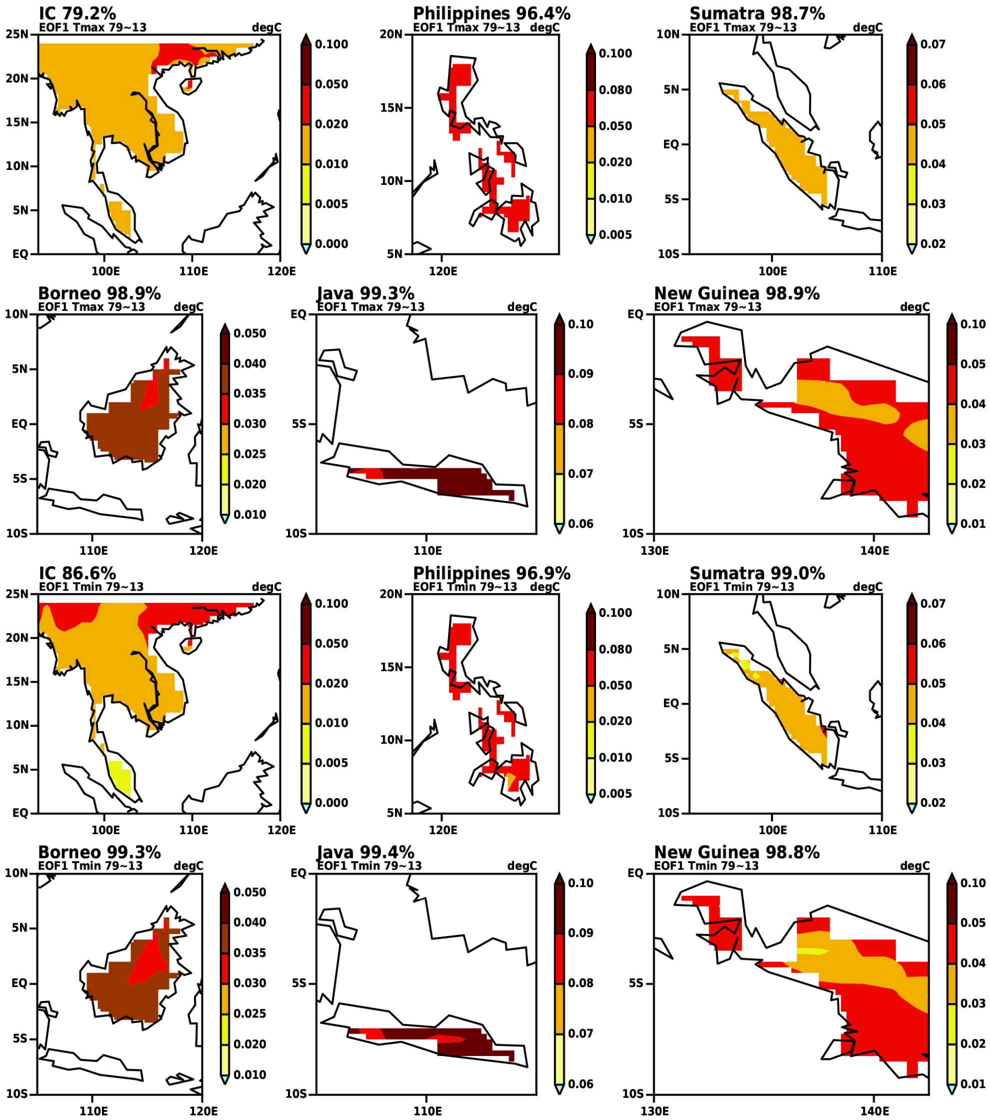


Figure 3 Leading EOF pattern of daily maximum and minimum temperatures (°C) from 1979 to2013. The upper six panels are for maximum temperature and the lower six panels are forminimum temperature.

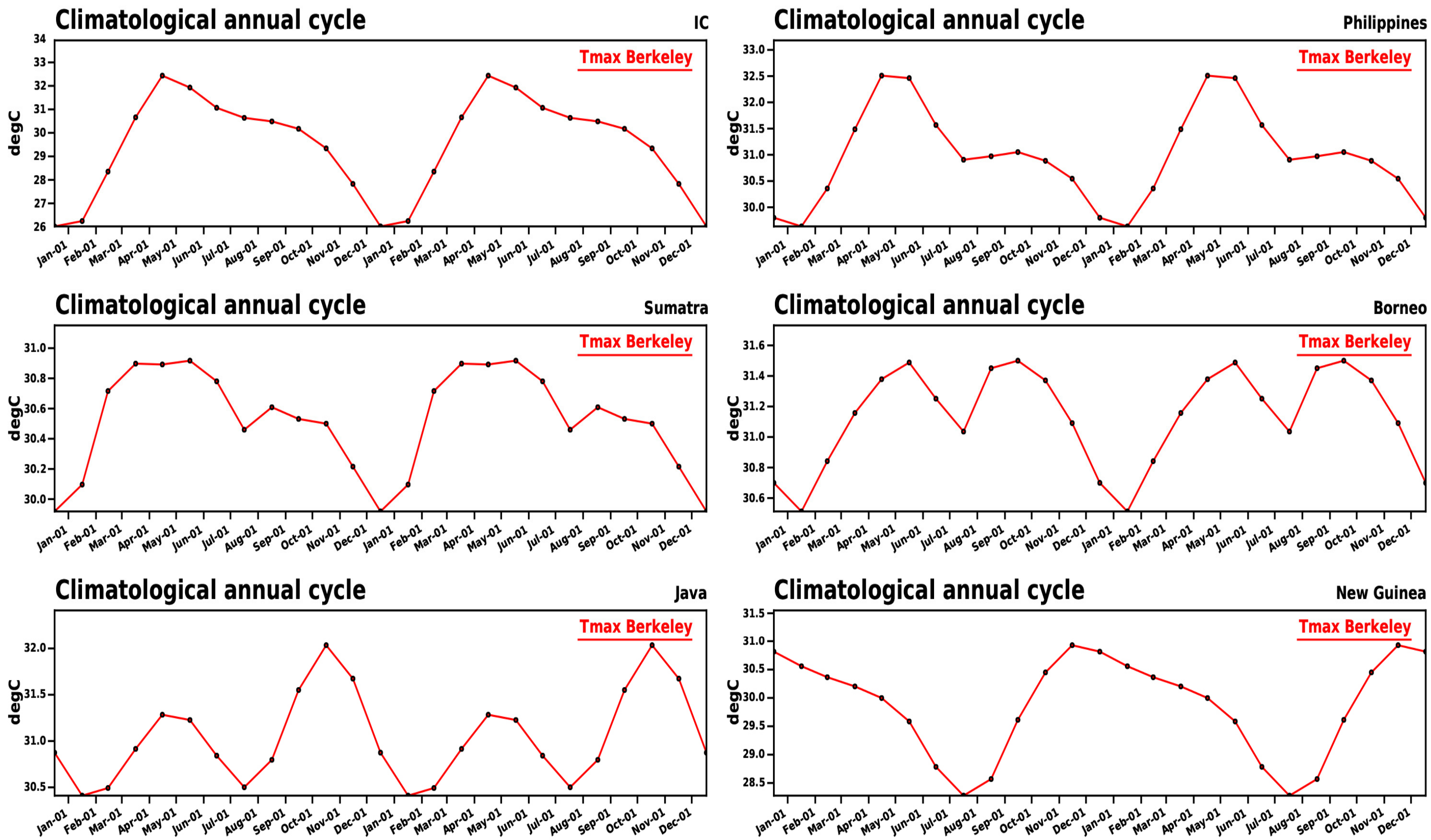


Figure 4 Monthly climatological annual cycle of maximum temperature over each of the six lands. Two cycles were plotted.

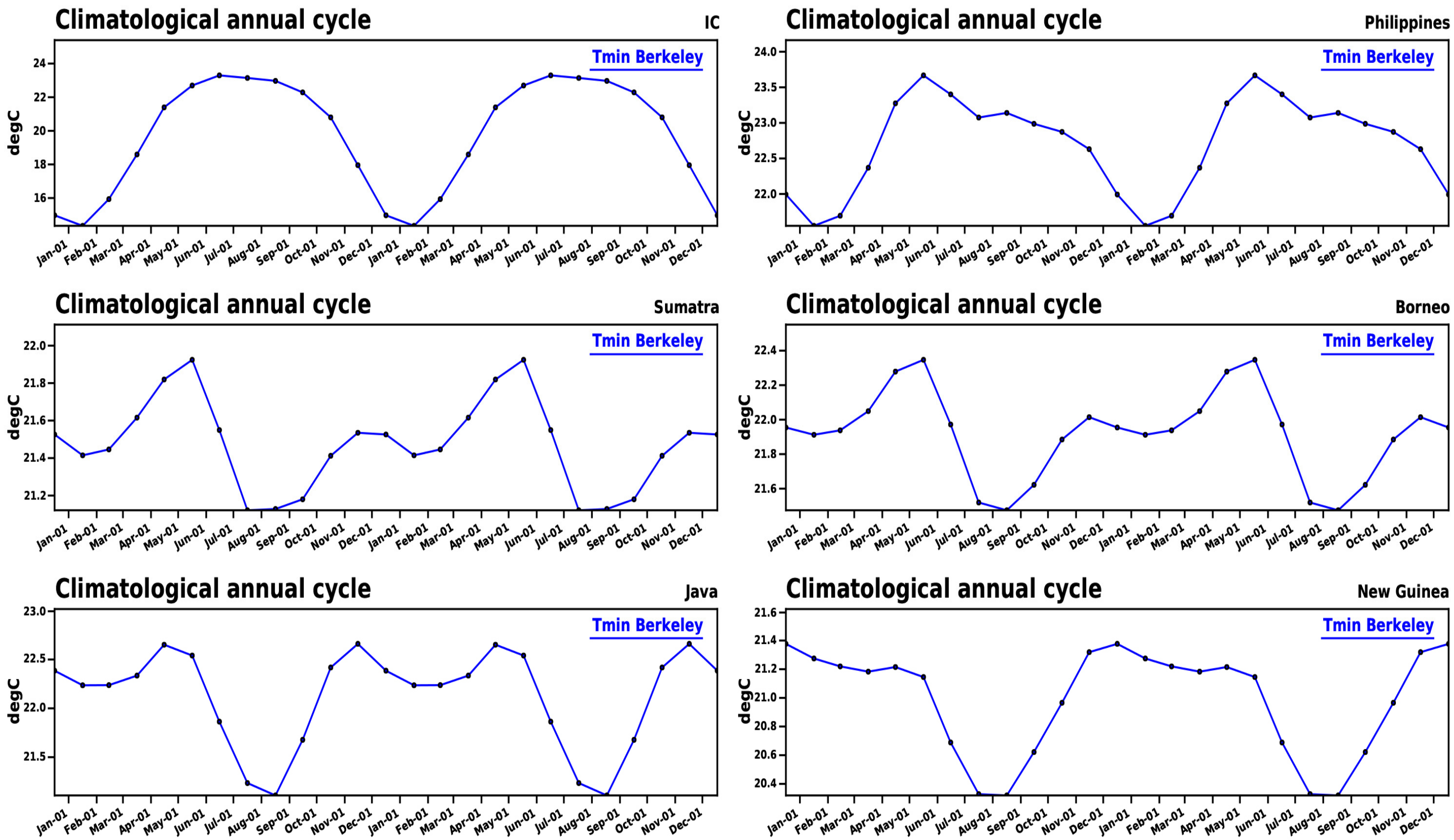


Figure 5 As Figure 4, but for minimum temperature.

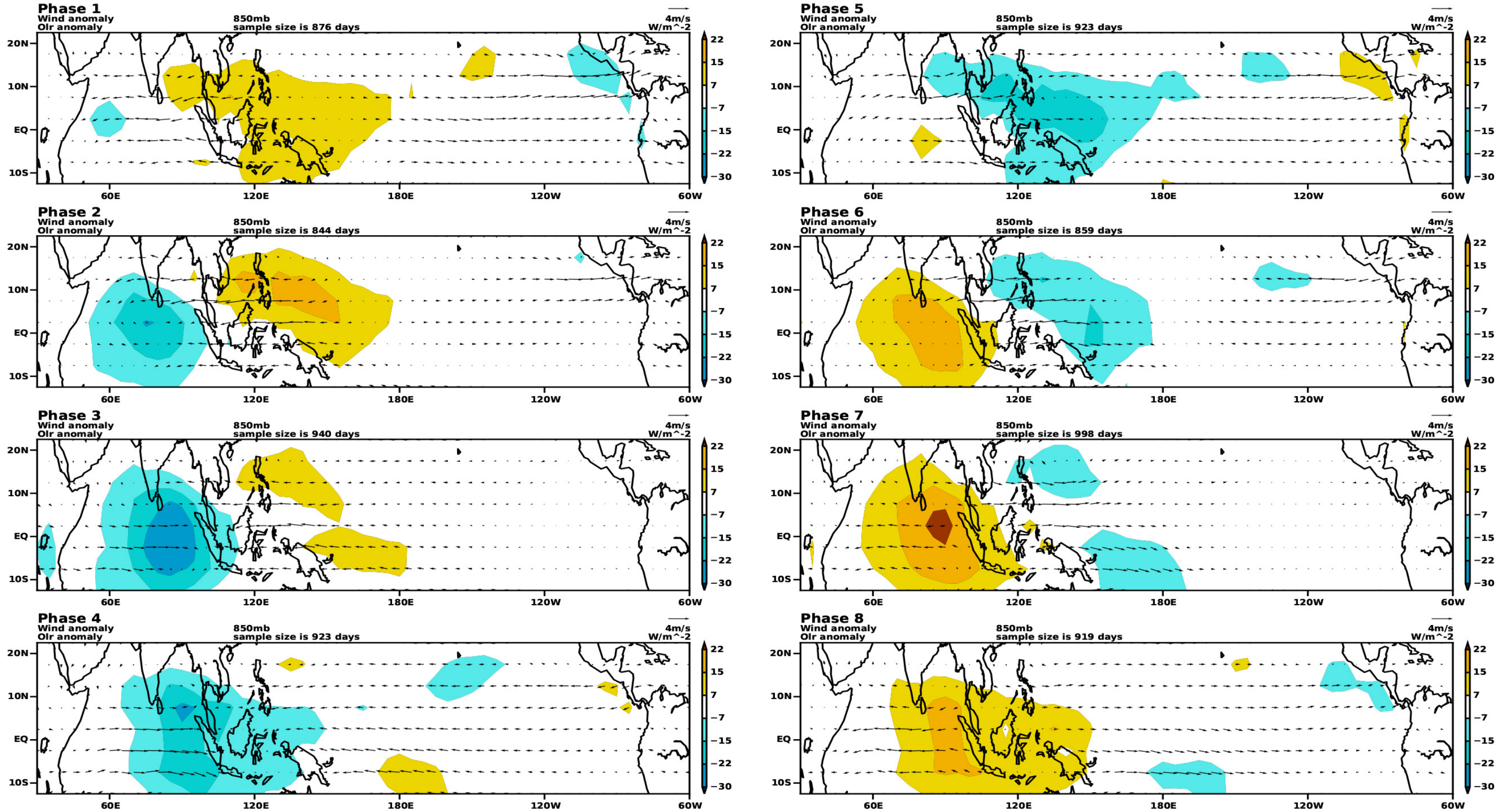


**Figure 6** MJO life cycle from multivariate EOF analysis. Shading shows the OLR anomaly (W/m$^2$). The vector is the horizontal wind anomaly at850 hPa.

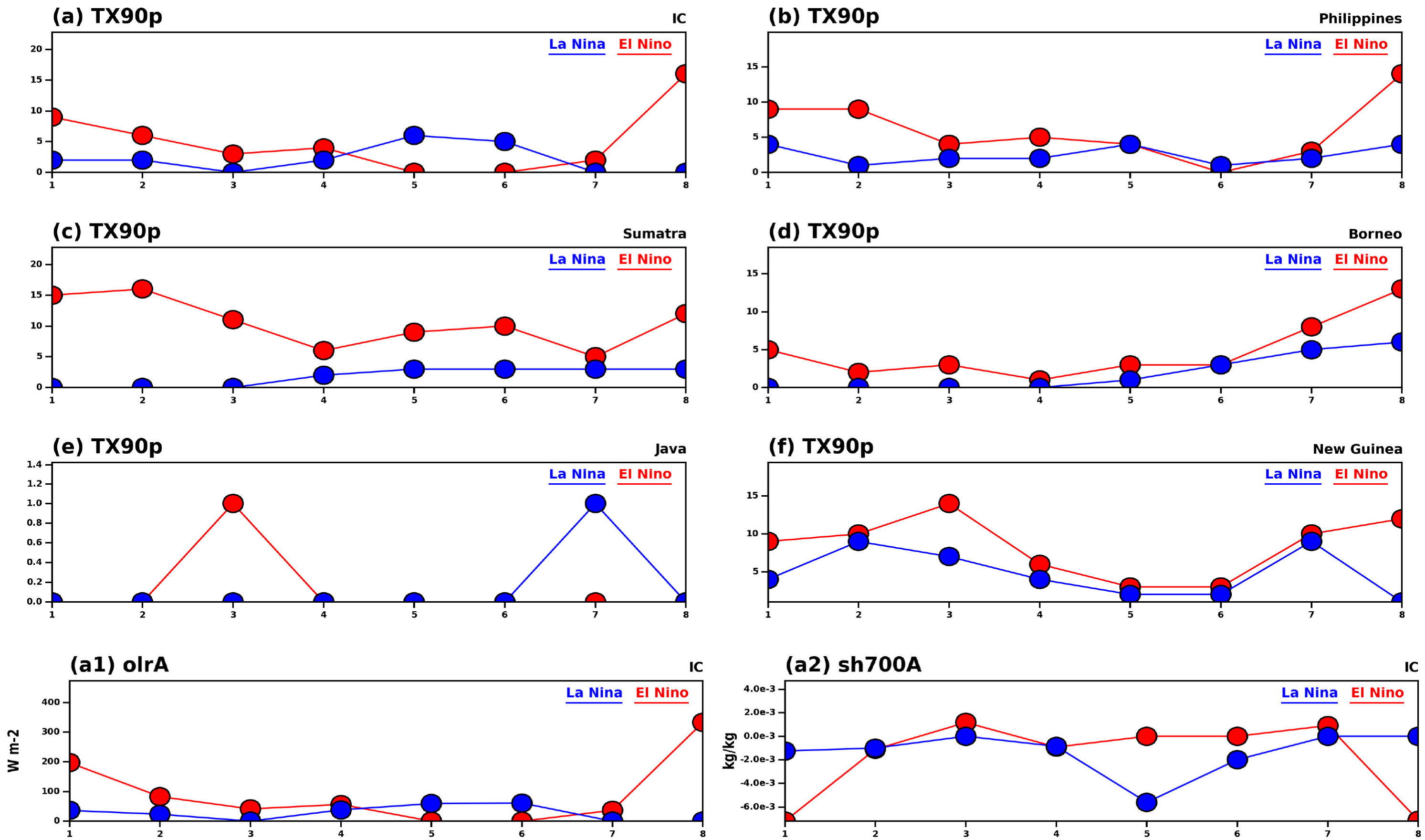


Figure 7 Composited TX90p as a function of eight MJO phases and two ENSO phases averaged over six lands (a–f). (a1) The composited accumulatedOLR anomaly as a function of MJO and ENSO phases averaged over IC. (a2) The the composited accumulated anomalous specific humidity at 700 hPaaveraged over IC.

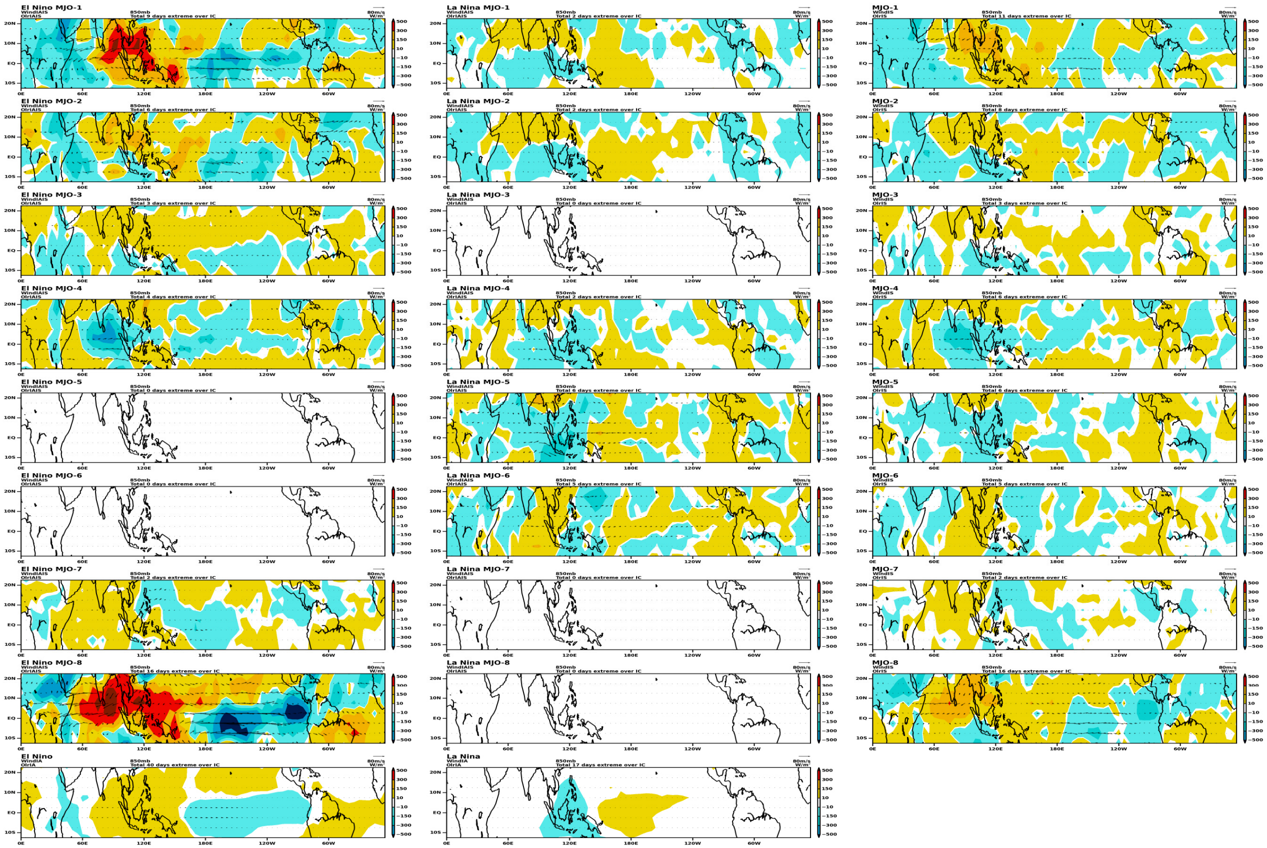


**Figure 8** Anomalous evolution of OLR and horizontal wind at 850 hPa as a function of MJO and ENSO conditional on TX90p over IC. The bottomrow of panels are the composited interannual variation of OLR and winds classified by ENSO phases. The right column is the compositedintraseasonal variation of OLR and wind classified by MJO phases. Other panels are the composited interannual and intraseasonal variation ofOLR and wind classified by ENSO in conjunction with MJO phases. Warm colors for OLR correspond to clear sky.

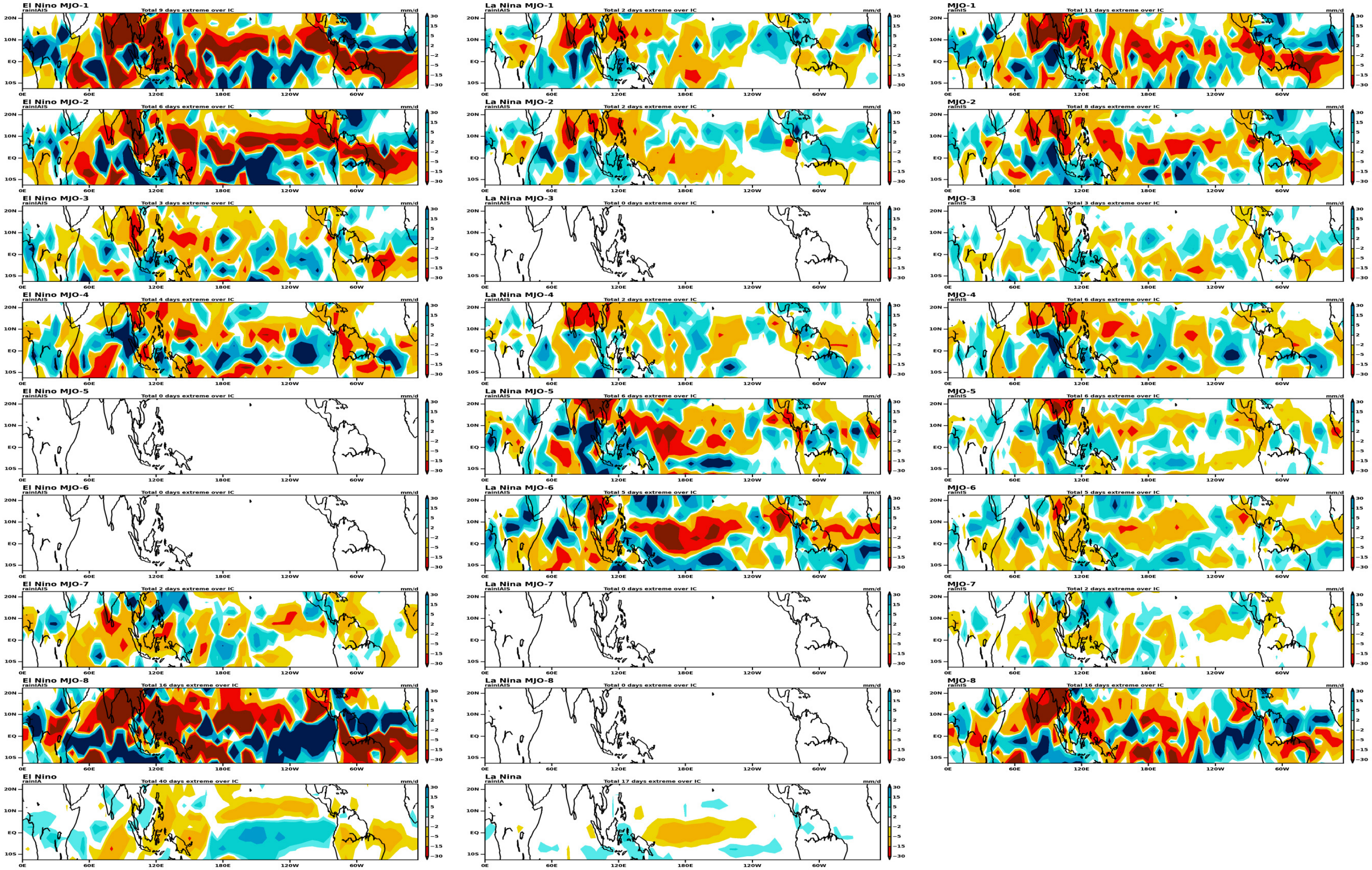


Figure 9 As Figure 8, but for rainfall.

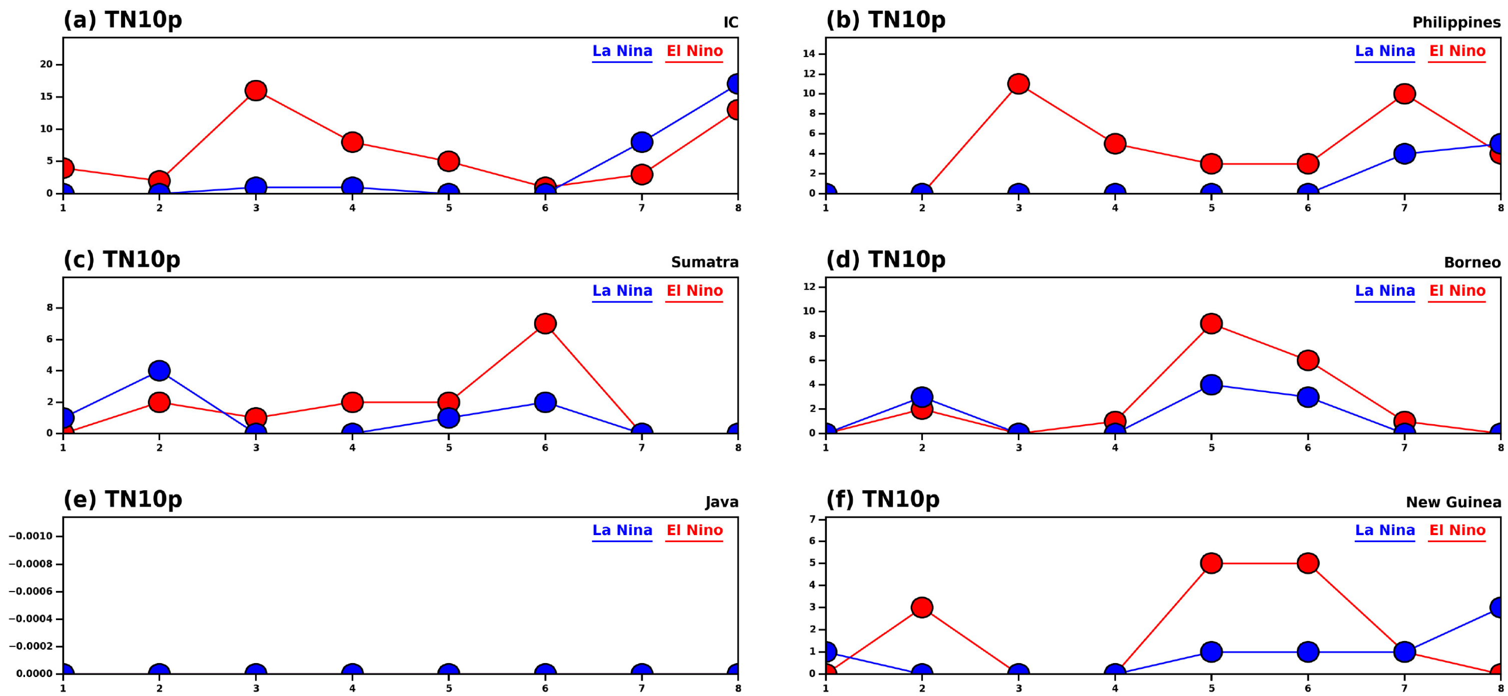


Figure 10 Composited TN10p as a function of eight MJO phases and two ENSO phases averaged over six lands (a–f).

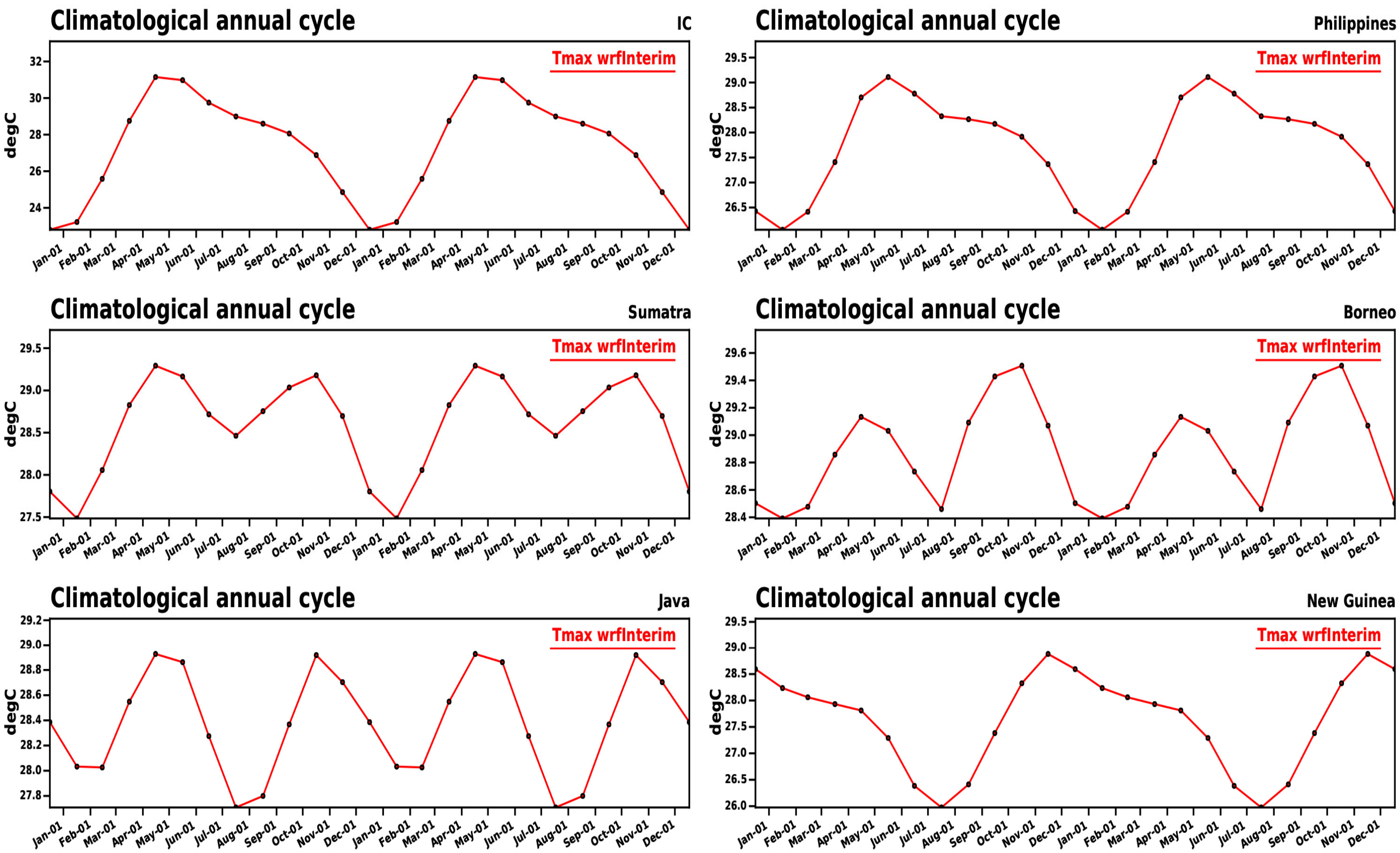


Figure 11 Monthly climatological annual cycle of maximum temperature simulated in the hindcast experiment. Two cycles were plotted.

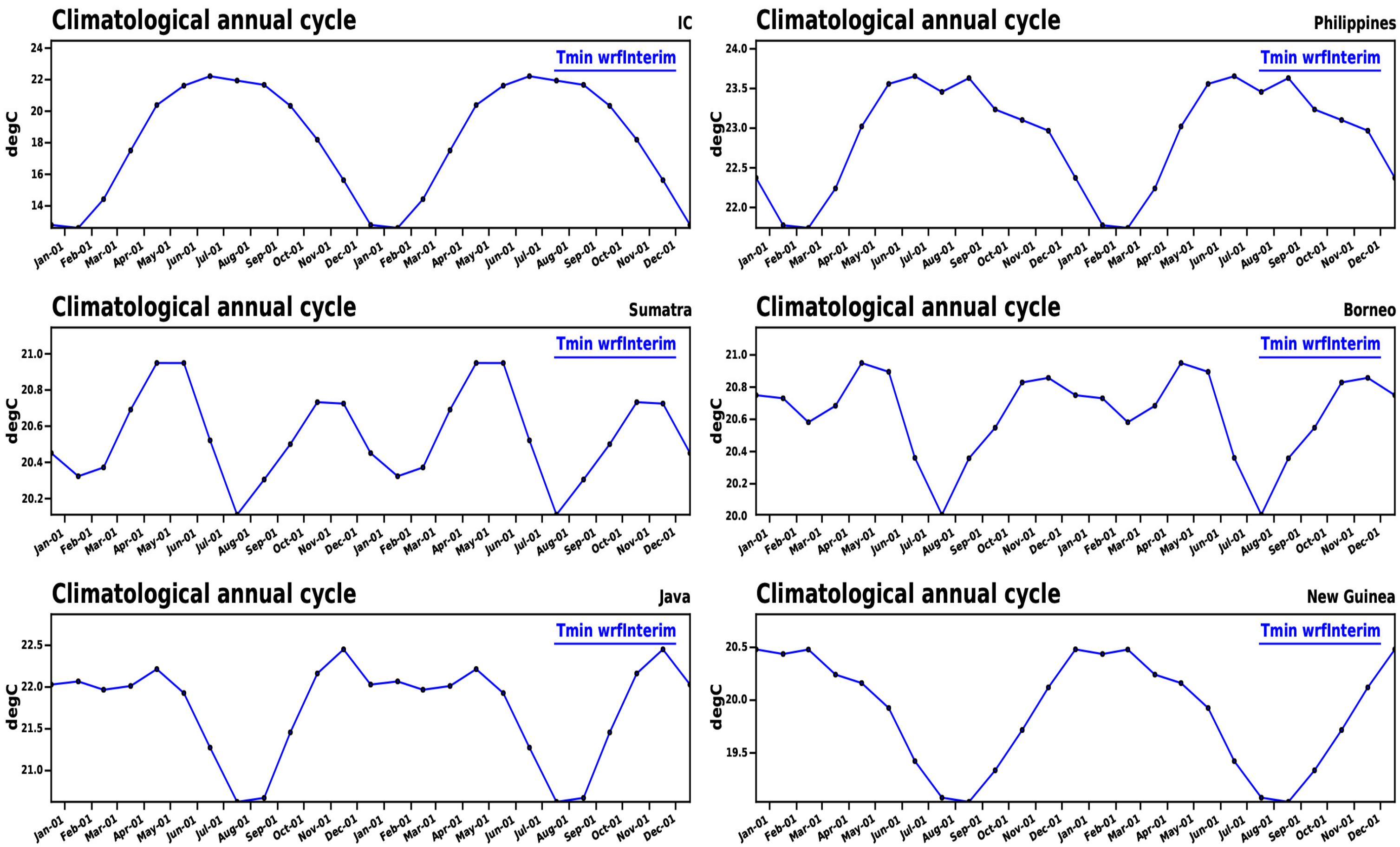


Figure 12 As Figure 11, but for minimum temperature.

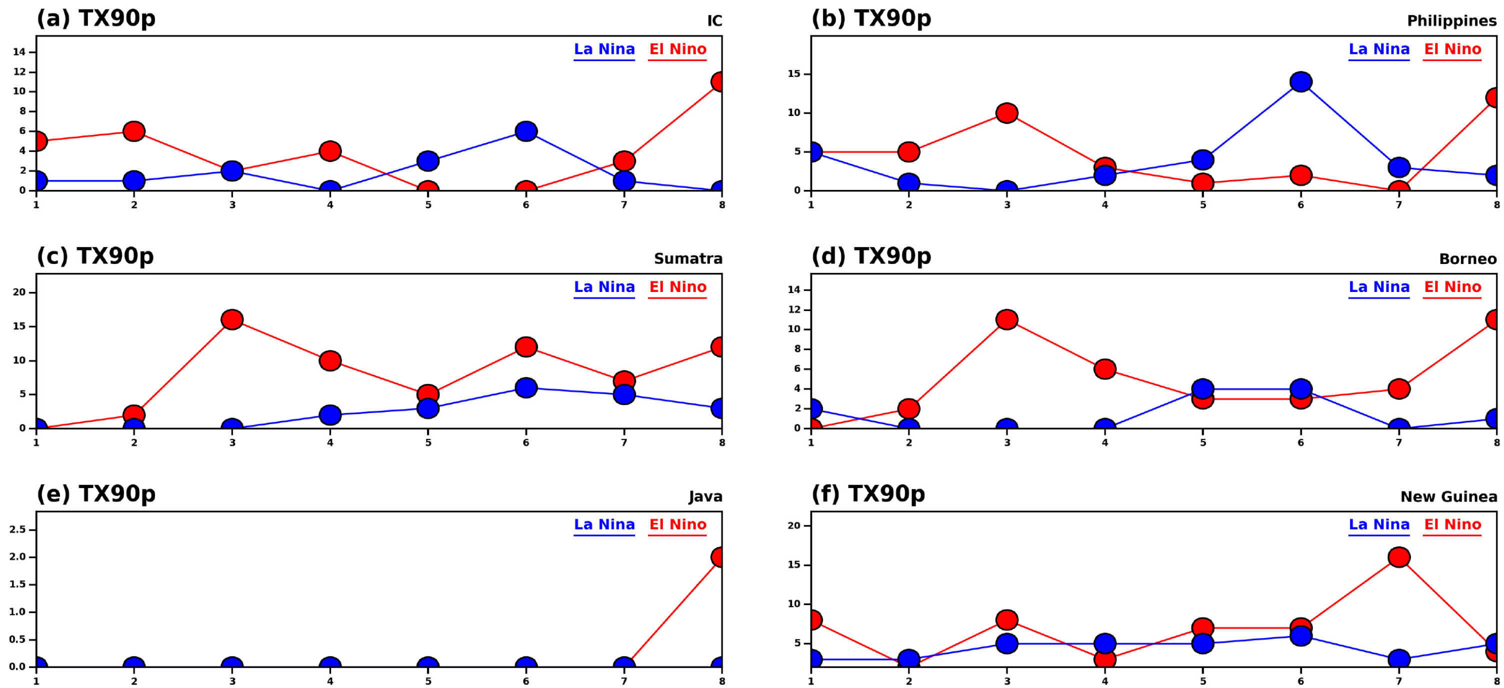


Figure 13 Composited TX90p as a function of eight MJO phases and two ENSO phases in the hindcast experiment.

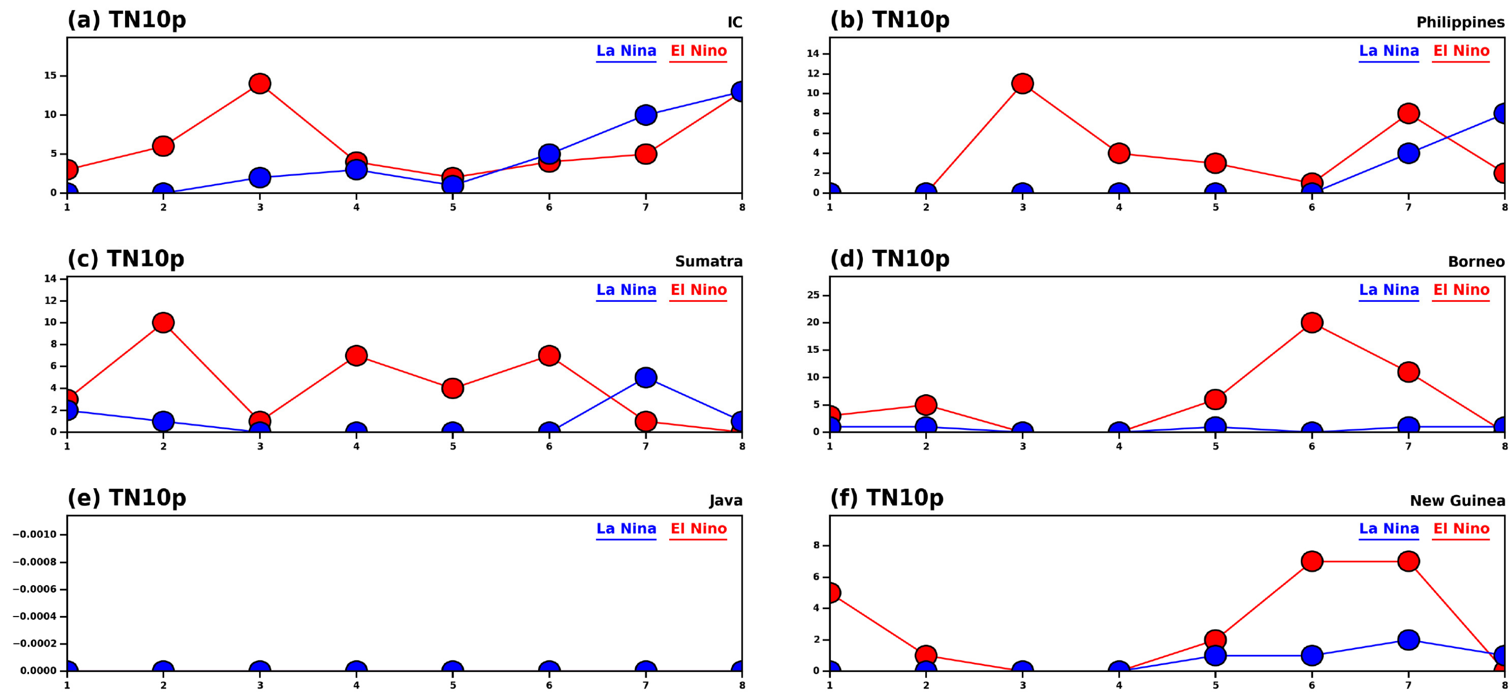


Figure 14 As Figure 13, but for TN10p.

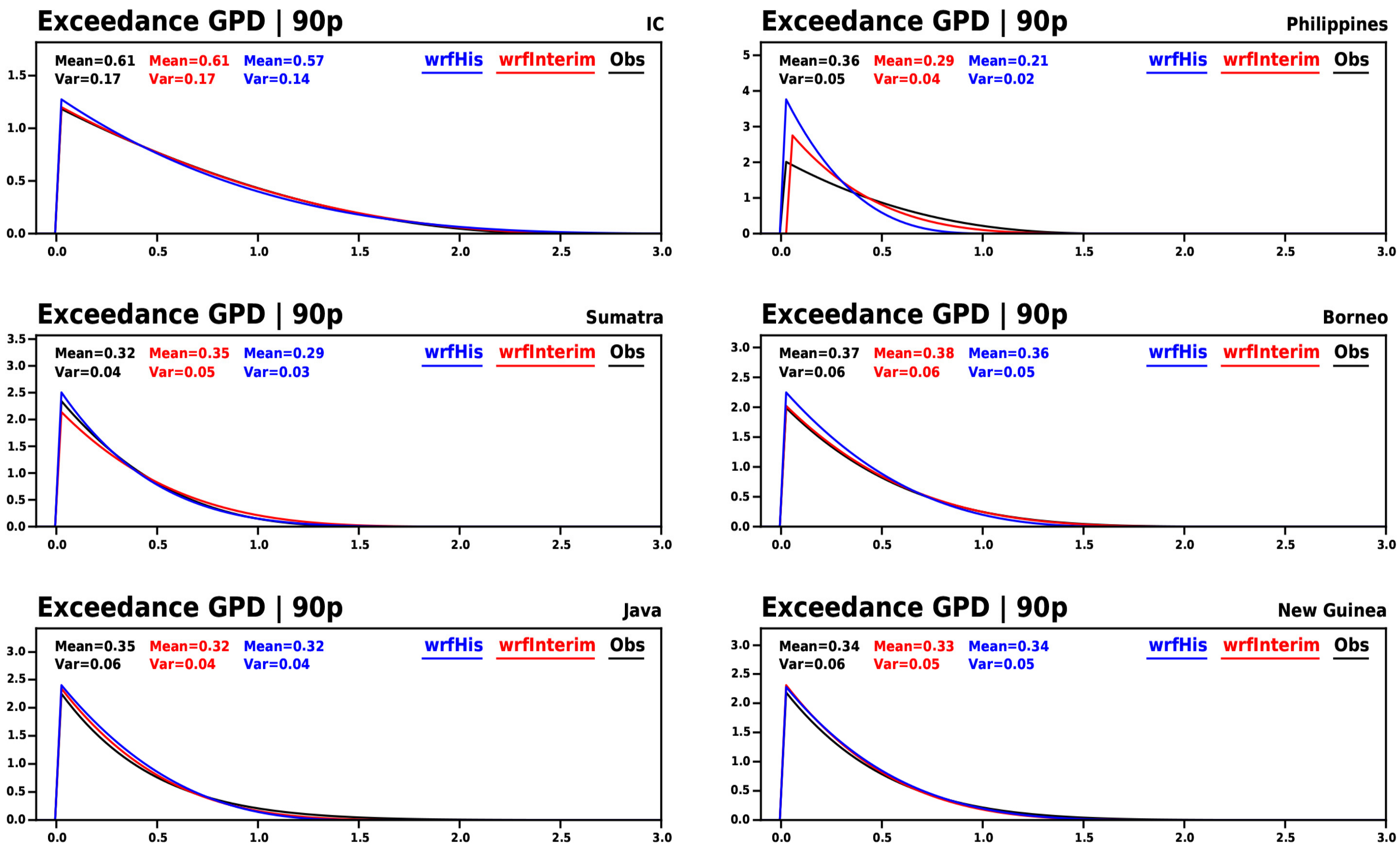


Figure 15 PDFs for the TX90p from the observations, hindcast experiments, and historical experiments over each land. The robust mean and robustvariation are shown in each panel.

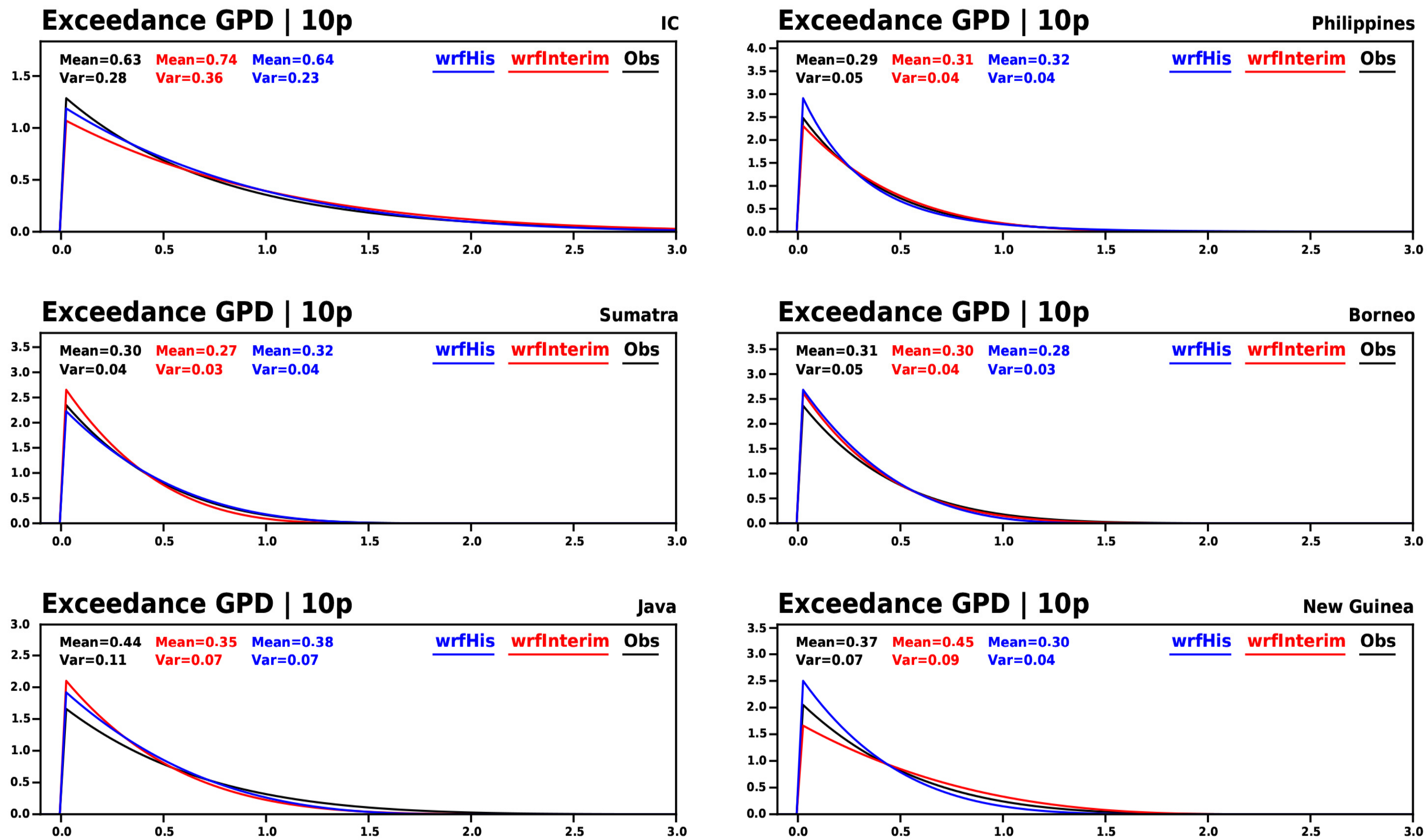


Figure 16 As Figure 15, but for TN10p.

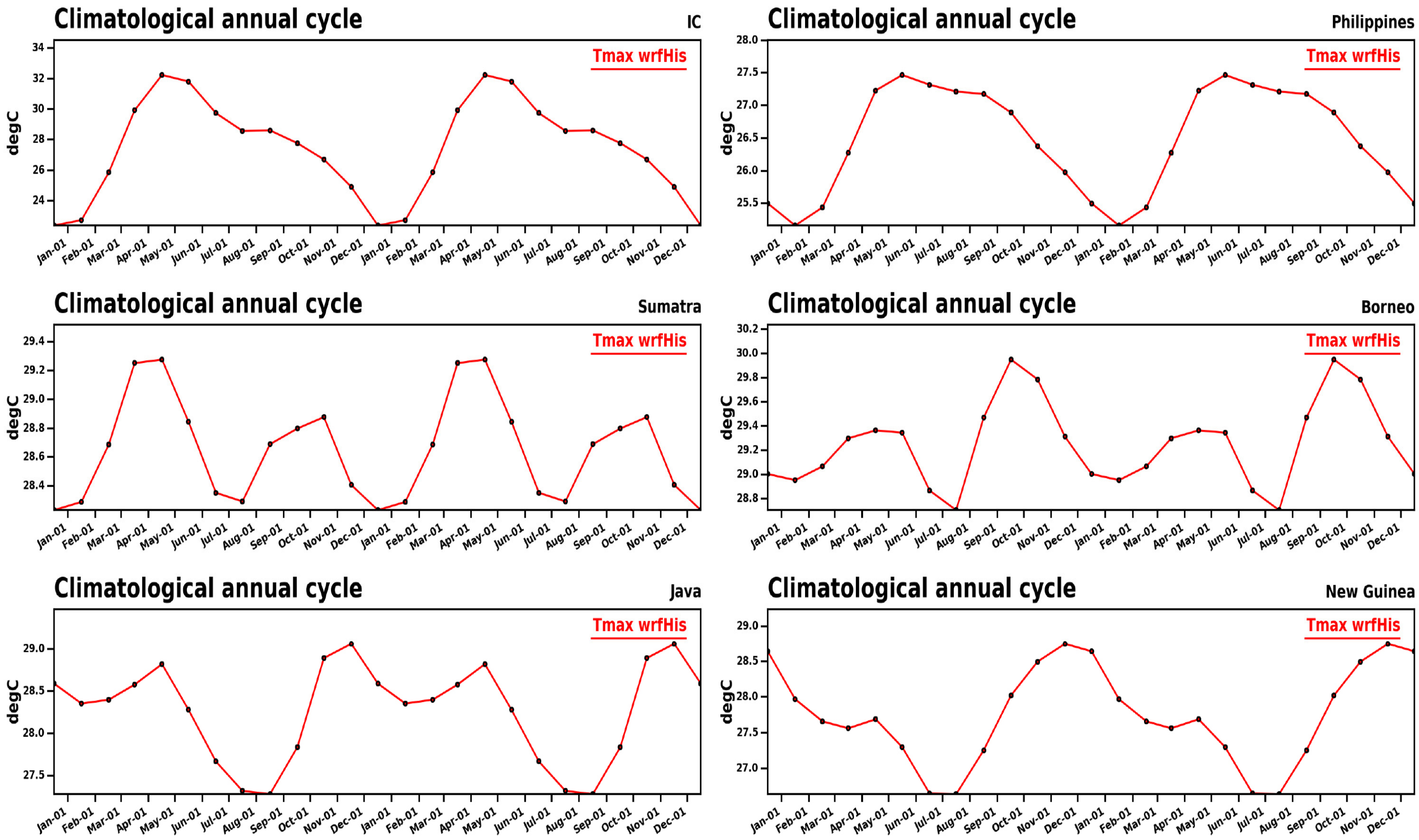


Figure 17 Monthly climatological annual cycle of maximum temperature simulated in the historical experiment. Two cycles were plotted.

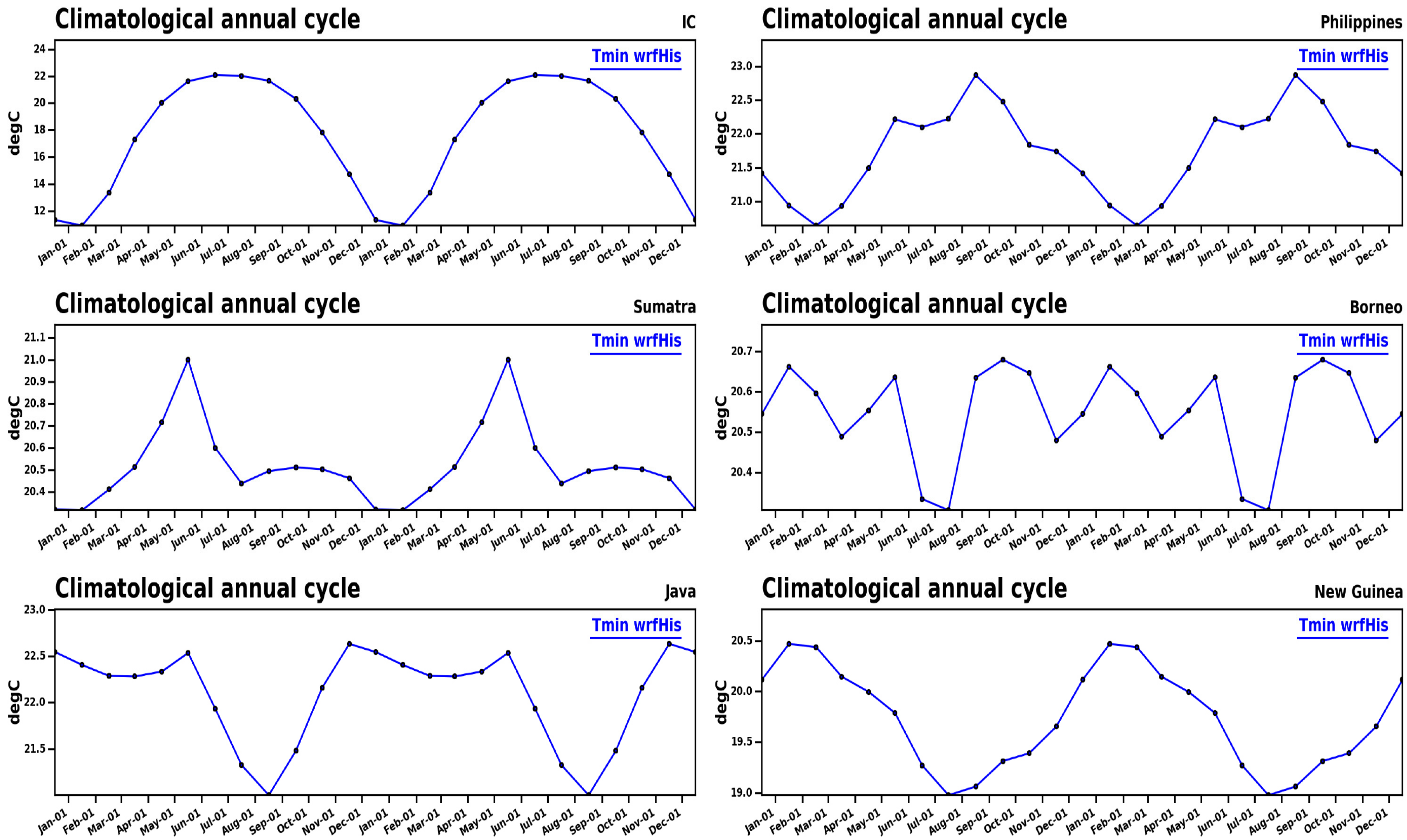


Figure 18 As Figure 17, but for minimum temperature.

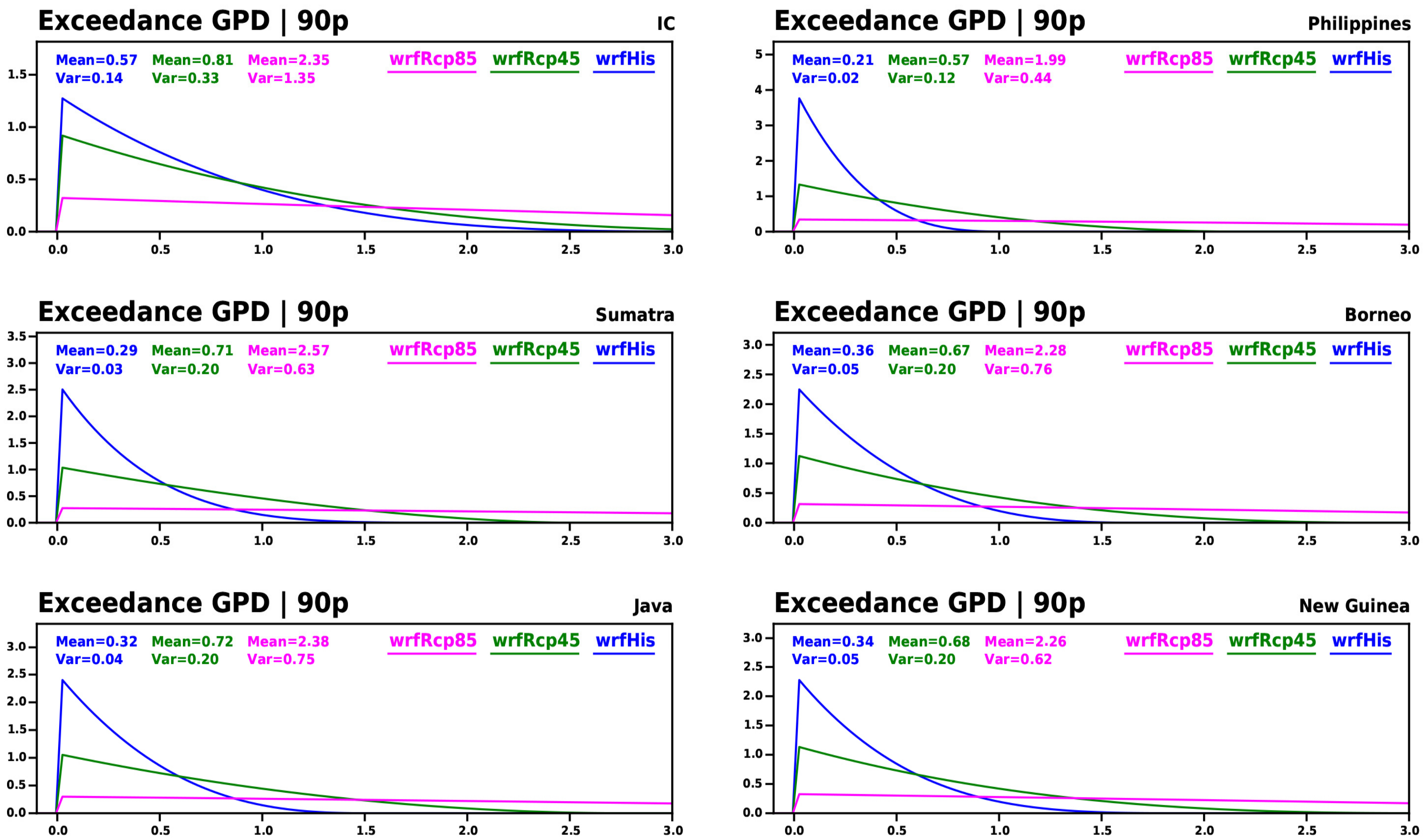


Figure 19 PDFs for TX90p from the historical, near future of Down-45, and the far future of Down-85 experiments over each land. The robust mean androbust variation are shown in each panel.

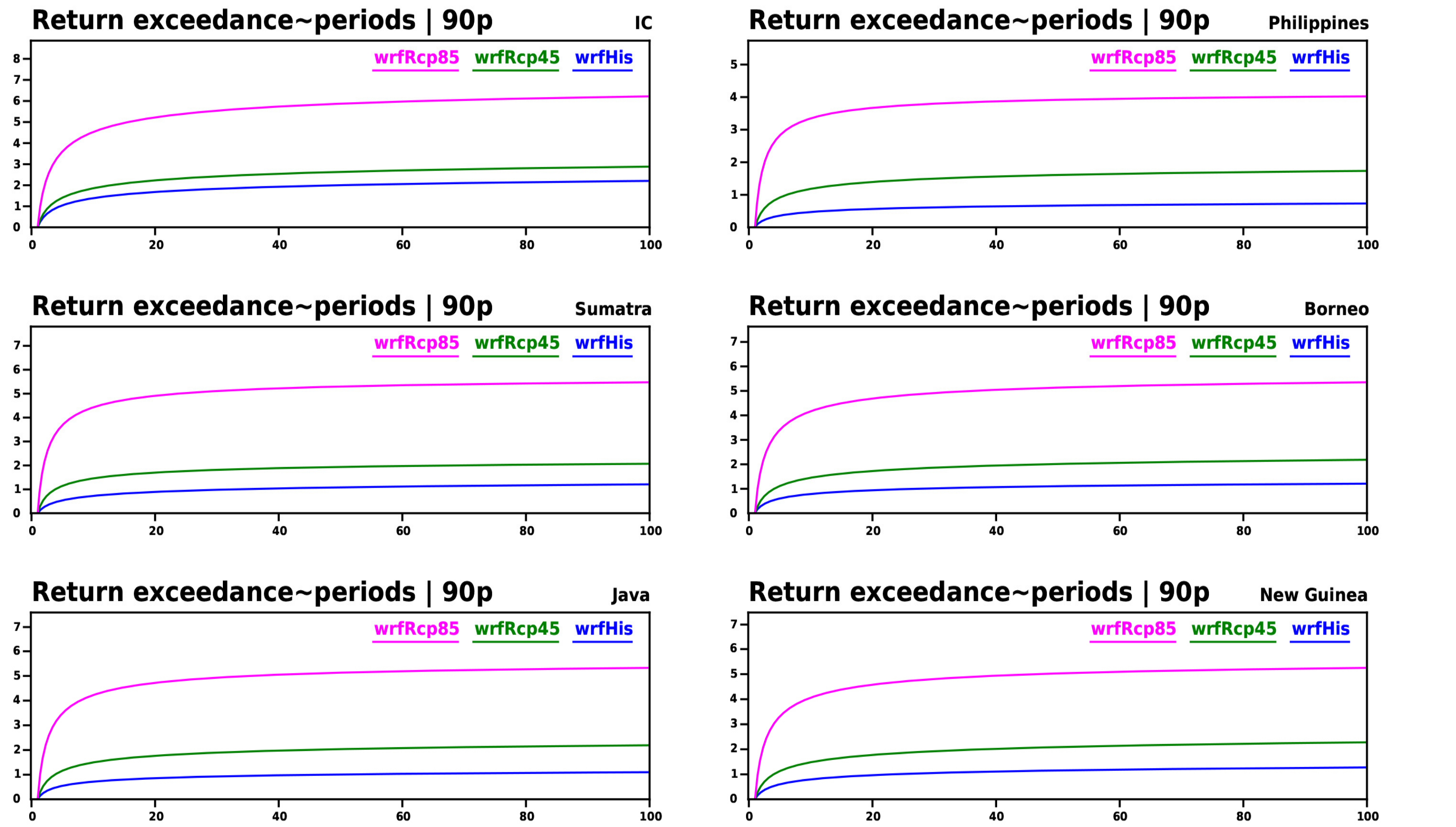


Figure 20 Return value versus return period for the historical experiment, Down-45 (RCP 4.5; 2021-2045), and Down-85 (RCP 8.5; 2071-2095) overeach land.

Research Report 2016-05

Variability of regional extreme temperature over the Maritime Continent

Hongwei Yang

APEC Climate Center
12 Centum 7-ro, Haeundae-gu, Busan 48058, Republic of Korea
Tel: +82-51-745-3900 Fax: +82-51-745-3949
www.apcc21.org

ISBN 979-11-5698-156-5